Critical time-step size analysis and mass scaling by ghost-penalty for immersogeometric explicit dynamics

Stoter, Stein K.F.; Divi, Sai C.; van Brummelen, E. Harald; Larson, Mats G.; de Prenter, Frits; Verhoosel, Clemens V.

DOI
10.1016/j.cma.2023.116074

Publication date
2023

Document Version
Final published version

Published in
Computer Methods in Applied Mechanics and Engineering

Citation (APA)
Stoter, S. K. F., Divi, S. C., van Brummelen, E. H., Larson, M. G., de Prenter, F., & Verhoosel, C. V. (2023). Critical time-step size analysis and mass scaling by ghost-penalty for immersogeometric explicit dynamics. *Computer Methods in Applied Mechanics and Engineering*, *412*, Article 116074. https://doi.org/10.1016/j.cma.2023.116074

Available online at www.sciencedirect.com
ScienceDirect
Comput. Methods Appl. Mech. Engrg. 412 (2023) 116074
Computer methods in applied mechanics and engineering
www.elsevier.com/locate/cma

Critical time-step size analysis and mass scaling by ghost-penalty for immersogeometric explicit dynamics

Stein K.F. Stoter[a,*], Sai C. Divi[a], E. Harald van Brummelen[a], Mats G. Larson[b], Frits de Prenter[c], Clemens V. Verhoosel[a]

[a] Department of Mechanical Engineering, Eindhoven University of Technology, The Netherlands
[b] Department of Mathematics and Mathematical Statistics, Umeå University, 901 87 Umeå, Sweden
[c] Department of Aerospace Engineering, Delft University of Technology, The Netherlands

Received 14 February 2023; received in revised form 25 March 2023; accepted 18 April 2023
Available online xxxx

Abstract

In this article, we study the effect of small-cut elements on the critical time-step size in an immersogeometric explicit dynamics context. We analyze different formulations for second-order (membrane) and fourth-order (shell-type) equations, and derive scaling relations between the critical time-step size and the cut-element size for various types of cuts. In particular, we focus on different approaches for the weak imposition of Dirichlet conditions: by penalty enforcement and with Nitsche's method. The conventional stability requirement for Nitsche's method necessitates either a cut-size dependent penalty parameter, or an additional ghost-penalty stabilization term. Our findings show that both techniques suffer from cut-size dependent critical time-step sizes, but the addition of a ghost-penalty term to the mass matrix serves to mitigate this issue. We confirm that this form of 'mass-scaling' does not adversely affect error and convergence characteristics for a transient membrane example, and has the potential to increase the critical time-step size by orders of magnitude. Finally, for a prototypical simulation of a Kirchhoff–Love shell, our stabilized Nitsche formulation reduces the solution error by well over an order of magnitude compared to a penalty formulation at equal time-step size.

Keywords: Immersogeometric analysis; Explicit dynamics; Critical time step; Finite cell method; Ghost penalty; Mass scaling

1. Introduction

Explicit analysis forms the backbone of impact and crash-test simulation software. In these highly non-linear, short time-span simulations, the structure that is impacted is often comprised of shell-type components [1–3]. *Isogeometric analysis* has emerged as a framework that streamlines the design-to-analysis pipeline for these types of simulations [4–6]. In isogeometric analysis, the spline-based geometry representation from CAD drawings is used directly in the analysis software [4]. The higher-order continuity of the spline basis functions makes them particularly well-suitable for handling the higher-order partial differential equations that arise in shell-type formulations [6–8]. Additionally, for higher polynomial orders and non-open knot vectors, the increased regularity of splines

* Corresponding author.
E-mail addresses: K.F.S.Stoter@tue.nl (S.K.F. Stoter), S.C.Divi@tue.nl (S.C. Divi), E.H.v.Brummelen@tue.nl (E.H. van Brummelen), Mats.Larson@umu.se (M.G. Larson), F.d.Prenter@tudelft.nl (F. de Prenter), C.V.Verhoosel@tue.nl (C.V. Verhoosel).

https://doi.org/10.1016/j.cma.2023.116074

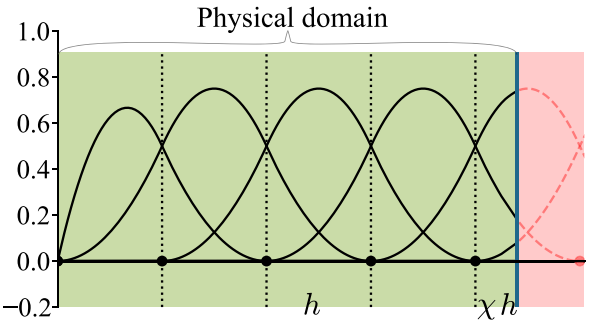

(a) Domain, basis functions and cut element. Green represents the physical domain interior, and red the exterior.

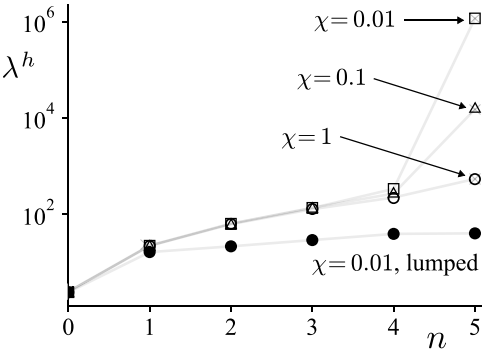

(b) Spectra for various element size fractions, with and without mass lumping.

Fig. 1. Effect of the small-cut elements (characterized by the element size fraction χ that is illustrated in Fig. 1(a)) on the eigenvalues of a rod discretized with the six basis functions depicted in Fig. 1(a), for consistent and row-sum lumped mass matrices.

suppresses the overprediction of the maximum eigenvalues that plague standard ($\mathcal{C}^0$-continuous) finite elements for fully-integrated mass-to-stiffness generalized eigenvalue problems [9,10]. The frequency spectra obtained for lower-order continuous basis functions exhibit (a multitude of) so-called optical branches [11], which exacerbate the approximation mismatch in the high-frequency segment of the spectrum and negatively affect the permissible time-step size of explicit time-stepping methods.

The spline geometry representation from CAD drawings often involves trimmed edges, where the physical domain boundary cuts through the computational background mesh. These "immersed boundary" methods, referred to as immersogeometric methods in the context of isogeometric analysis, have been extensively studied in recent years [12–17]. An example of a one-dimensional immersogeometric discretization is shown in Fig. 1(a), where the B-spline basis functions are not confined to the physical domain. The size of the cut is characterized by the elements size fraction χ. The presence of basis functions with small support within the physical domain, i.e., with small χ, negatively impacts the stability characteristics of the numerical scheme. In implicit analysis, these issues manifest themselves as poor conditioning of the resulting system of equations [18]. For explicit analysis, a primary concern is the effect of small cut elements on the maximum eigenvalue, λ^h_{max}, of the mass-to-stiffness generalized eigenvalue problem. Indeed, for a one-dimensional rod example with the basis functions from Fig. 1(a), the cut-size heavily affects the maximum eigenfrequency, as can be observed from the diverging open markers in Fig. 1(b). For explicit time-stepping methods, an increase in the maximum eigenfrequency leads to a tighter bound on the magnitude of the permissible time step. The specific relation between λ^h_{max} and this so-called "critical time-step size", Δt_{crit}, depends on the explicit time-integration technique that is employed. A typical example for undamped structural dynamics is

$$\Delta t_{\text{crit}} = \frac{2}{\sqrt{\lambda^h_{\text{max}}}}, \tag{1}$$

which holds for the Newmark-type central difference method [19, p. 493].

The diverging results of the open markers in Fig. 1(b) are obtained for a "full" or "consistent" mass matrix (in the sense of [20]) in the formulation of the eigenvalue problem. In explicit analysis, the practice of mass diagonalization through some form of mass lumping is the gold standard [19], as this is essential to attaining a fast solver. As can be observed from the filled marker in Fig. 1(b), the use of such a (row-sum) lumped mass matrix completely mitigates the detrimental impact of small cuts. This was first observed by Leidinger et al. [21], where this behavior is explored analytically in one dimension, and numerically in two dimensions.

The non-boundary fitted nature of immersed methods also requires specialized techniques for enforcing essential boundary conditions. Often, penalty-based methods are employed. In the context of explicit dynamics, not only the relation between the penalty parameter and the solution quality needs to be understood, but also its impact on the maximum eigenvalue. This is explored in the immersogeometric framework in [5,21], where the authors report that

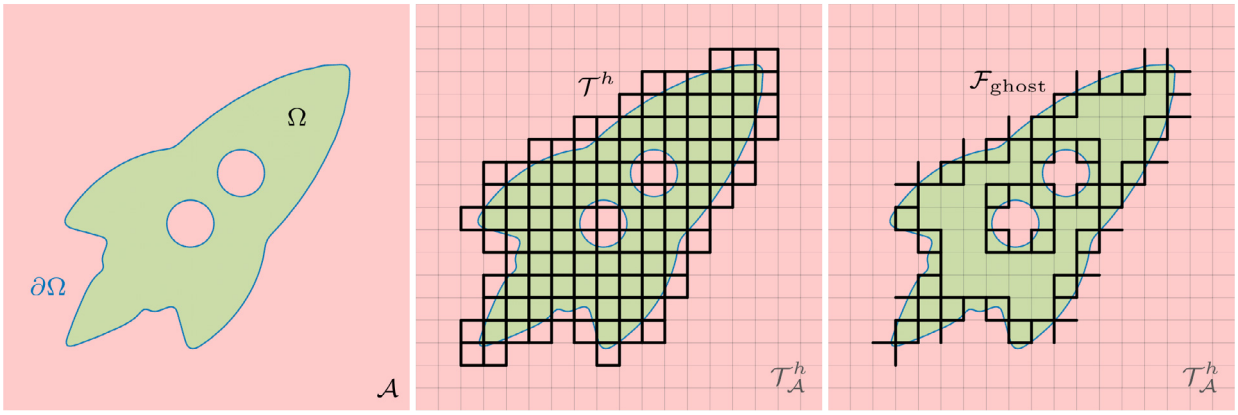

(a) Ambient and physical domain. **(b)** Ambient and background mesh. **(c)** Ghost faces.

Fig. 2. Definitions of the different meshes and domains in the immersed setting.

sufficient solution accuracy can be attained with a penalty parameter that is small enough to avoid affecting the largest eigenvalue. When the penalty parameter exceeds a certain limit, the maximum eigenvalue scales linearly with the penalty parameter. The same linear scaling is observed for Nitsche's method in [22].

The current work aims to study the impact of small cuts on the critical time-step size in a wider range of scenarios, by investigating second- and fourth-order partial differential equations, regardless of the spatial dimension and polynomial order of the discretization, and considering various penalty- and Nitsche-based formulations for enforcing Dirichlet conditions. We also explore the use of ghost-penalty-based stabilization of the stiffness [23,24] and/or mass matrix [25,26]. Our goal is to identify the appropriate formulations in the explicit immersogeometric setting, and to evaluate the potential benefits of the alternative formulations in typical explicit dynamics computations.

The remainder of this article is structured as follows. In Section 2, we present the theory and nomenclature relevant to the topic of immersogeometric methods. We then focus on a linear wave equation in Section 3, where we systematically collect the contributions to the mass and stiffness matrices for various immersed boundary formulations. Once the general formulation is derived, we analytically derive minimal scaling-orders of the maximum eigenvalue with respect to the cut-element size. This analysis is repeated for a linear fourth-order equation in Section 4. The results obtained are experimentally verified in Section 5, where we also perform convergence studies for the linear wave equation, and transient simulations of a linear Kirchhoff–Love shell model. Finally, in Section 6, we present our concluding remarks.

2. Immersogeometric methods

Consider a physical domain $\Omega \subset \mathbb{R}^d$ ($d \in \{2, 3\}$) and its boundary $\partial\Omega$, immersed in an ambient domain $\mathcal{A} \supset \Omega$, as shown in Fig. 2(a). The ambient mesh $\mathcal{T}^h_{\mathcal{A}}$ is a structured mesh covering the ambient domain $\mathcal{A}$. The "background mesh" is then defined as the collection of elements from the ambient mesh that intersect the physical domain:

$$\mathcal{T}^h := \left\{ K \in \mathcal{T}^h_{\mathcal{A}} : K \cap \Omega \neq \emptyset \right\}. \tag{2}$$

Both the ambient mesh and the background mesh are illustrated in Fig. 2(b).

We also define a set of "ghost faces" as the collection of faces of elements from the background mesh that are intersected by the domain boundary:

$$\mathcal{F}_{\text{ghost}} = \left\{ \partial K \cap \partial K' \ : \ K \in \mathcal{G}, K' \in \mathcal{T}^h, K \neq K' \right\}, \tag{3}$$

where $\mathcal{G} := \{K \in \mathcal{T}^h \mid K \cap \partial\Omega \neq \emptyset\}$. The ghost faces are illustrated in Fig. 2(c).

2.1. Non-boundary fitted B-spline basis functions

The structured nature of the ambient mesh allows for the straightforward construction of multivariate B-spline basis functions as tensor products between univariate B-spline functions. The left column in Fig. 3 depicts various

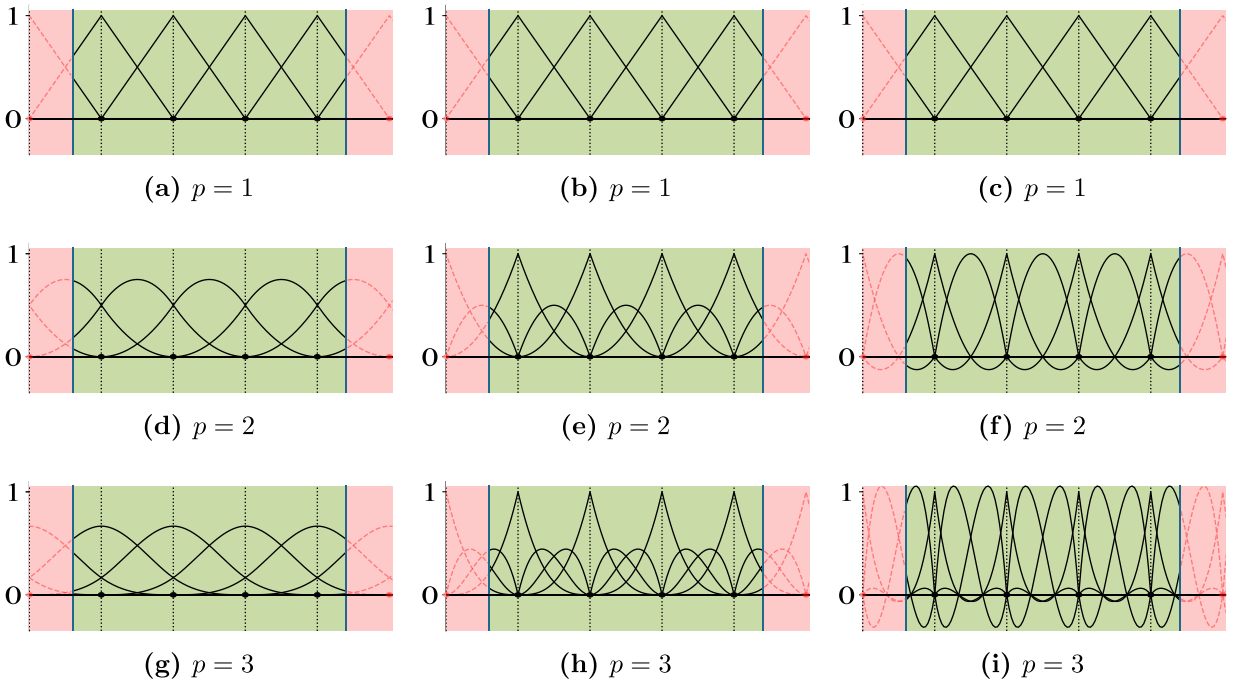

Fig. 3. Immersed $\mathcal{C}^{p-1}$-continuous B-splines (left), $\mathcal{C}^0$-continuous B-splines (middle) and standard $\mathcal{C}^0$-continuous Lagrange basis functions (right).

orders of univariate B-spline functions of maximum regularity, while the middle column shows C^0-continuous univariate B-spline functions. An important property of these B-spline basis functions is their non-negativity, meaning that the integral value of each of these functions on any arbitrary subdomain is naturally non-negative as well. The same is not true for the conventional $\mathcal{C}^0$-continuous Lagrange basis functions, as shown in the right column of Fig. 3. This non-negativity property is particularly important in the context of explicit dynamics, as it guarantees positivity of the diagonal components of the row-sum lumped mass matrix, which will be addressed in Section 3.1.2.

In this article, we focus on maximum regularity B-splines and address lower-order regularity cases only in remarks. For maximum regularity B-splines, each multivariate basis function $B_i(\boldsymbol{x})$ $(i = 1, \ldots, J)$ on the background mesh is a member of $\mathcal{C}^{p-1}(\mathcal{A})$, where p is the polynomial order of the B-spline. The precise construction of the tensor product B-spline functions can be found, for example, in [4]. To obtain the approximation space only on the physical domain, we first identify a subset of the maximum regularity B-splines that have non-zero support in the interior of the domain:

$$S = \left\{ N \in \{B_i(\boldsymbol{x})\}_{i=1}^{J} : \mathrm{supp}_{\Omega}(N) \neq 0 \right\}. \tag{4}$$

We then number the remaining functions in this set from $i = 1$ to N_{dofs}, and define the N_{dofs}-dimensional approximation space V^h as their span:

$$V^h = \mathrm{span}\,(S) = \mathrm{span}\left\{ N_i(\boldsymbol{x}) \right\}_i^{N_{\mathrm{dofs}}}. \tag{5}$$

Under the assumption that the approximation functions evolve smoothly from time $t = 0$ to time $t = T$, the time-dependent functions belong to the following semi-discrete function space:

$$V_T^h = V^h \otimes \mathcal{C}^{\infty}(0, T). \tag{6}$$

2.2. Integration of cut elements

For immersed finite element methods, integration procedures are crucial for capturing the physical geometry in the discrete formulation. The octree subdivision integration strategy, described in [27], is a widely used approach

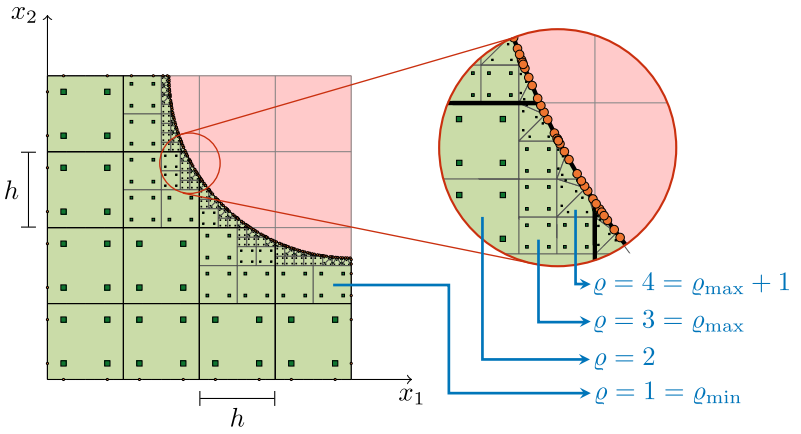

Fig. 4. Volumetric (squares) and surface (circles) quadrature rules obtained by the octree integration procedure with tessellation at the lowest bisectioning level.

due to its simplicity and robustness. However, the resulting large number of integration points may cause a significant computational cost increase during operation. A myriad of techniques to enhance octree-subdivision has been developed [28]. A few prominent techniques include error-estimate-based adaptive octree-subdivision [29], moment-fitting [30], equivalent polynomial methods [31], and the merged sub-cell technique [32].

In this article, we make use of the octree subdivision algorithm augmented with a tessellation step [33]. This approach consists of the following steps, as illustrated in Fig. 4: elements in the background mesh that intersect the boundary of the computational domain are bisected into 2^d sub-cells. If a sub-cell lies entirely within the domain, it is retained in the partitioning of the cut-cell, whereas it is discarded if it lies entirely outside the domain. This bisectioning procedure is recursively applied to the sub-cells that intersect the boundary, until $\varrho_{\max}$-times bisected sub-cells are obtained. At the lowest bisectioning level, a boundary tessellation procedure is applied to construct a $\mathcal{O}(h^2/2^{2\varrho_{\max}})$ accurate parametrization of the interior volume [33]. This tessellation procedure also provides a parametrization for the trimmed surface. The employed tessellation procedure is further detailed in [28].

The octree procedure results in integration rules on each of the sub-cells and each of the surface triangles. Cut-element volumetric integration is then performed by agglomerating all sub-cell quadrature points, and cut-element surface integration by collecting all triangulated surface quadrature points. The accuracy of the cut-element integration scheme can be controlled through the selection of the octree depth $\varrho_{\max}$ and the quadrature rules on the sub-cells. A two-dimensional illustration of the cut-element integration scheme is shown in Fig. 4, with the volumetric integration points represented by dark-green squares and the surface integration points depicted as orange circles.

3. Critical time-step analysis for a second-order problem

We center the exposition of our critical-timestep study for second-order initial/boundary-value problems around the linear wave equation:

$$\rho \frac{\partial^2}{\partial t^2}\phi - \nabla \cdot (\kappa \nabla \phi) = f \qquad \text{in } \Omega \times (0,T)\,, \tag{7a}$$

$$-\kappa \nabla \phi \cdot \boldsymbol{n} = g \qquad \text{on } \partial\Omega_N \times (0,T)\,, \tag{7b}$$

$$\phi = \phi_D \qquad \text{on } \partial\Omega_D \times (0,T)\,, \tag{7c}$$

$$\phi = \phi_0 \qquad \text{on } \Omega \times \{0\}\,, \tag{7d}$$

$$\frac{\partial}{\partial t}\phi = \dot{\phi}_0 \qquad \text{on } \Omega \times \{0\}\,, \tag{7e}$$

where ϕ is the unknown field, ρ and κ are parameters of the propagating medium, f, g, ϕ_D, ϕ_0 and $\dot{\phi}_0$ are the prescribed body force, Neumann data, Dirichlet data and initial state, respectively, $\Omega \subset \mathbb{R}^d$ and $T > 0$ are the spatial domain and final time, and $\partial\Omega_N$ and $\partial\Omega_D = \partial\Omega \setminus \partial\Omega_N$ are the Neumann and Dirichlet segments of the domain boundary.

This equation describes, for example, the out-of-plane displacement of a pre-stressed vibrating string or membrane in one, respectively two, dimensions, and the propagation of pressure waves in one, two or three dimensions. A weak formulation of this initial–boundary value problem reads [34]:

For a.e. $t \in (0, T)$, find $\phi \in H^1_{\phi_D}(\Omega)$ and $\frac{\partial^2}{\partial t^2}\phi \in H^{-1}(\Omega)$ s.t. $\forall\, v \in H^1_0\,\Omega$:

$$\begin{cases} \langle \frac{\partial^2}{\partial t^2}\phi,\, \rho\, v\rangle + \int_\Omega \kappa \nabla\phi \cdot \nabla v \,\mathrm{d}\Omega = \int_\Omega f\, v \,\mathrm{d}\Omega - \int_{\partial\Omega_N} g\, v \,\mathrm{d}S\,, \\ \phi\big|_{t=0} = \phi_0\,, \\ \frac{\partial}{\partial t}\phi\big|_{t=0} = \dot{\phi}_0\,, \end{cases} \tag{8}$$

where $H^1_{\phi_D}(\Omega) = \{\phi \in H^1(\Omega) : \phi\big|_{\partial\Omega_D} = \phi_D\}$, $H^{-1}(\Omega)$ is the corresponding dual space, and $\langle\cdot,\cdot\rangle$ denotes the pairing between them. If the second time derivative of ϕ is a member of $L^2(\Omega)$, then $\langle \frac{\partial^2}{\partial t^2}\phi,\, \rho\, v\rangle = \int_\Omega \rho \frac{\partial^2}{\partial t^2}\phi\, v \,\mathrm{d}\Omega$.

3.1. Semi-discrete formulation

With the aim of constructing a stable explicit finite element approximation for the weak formulation of Eq. (8) on a non-boundary-fitted isogeometric mesh, we consider the (semi-)discrete spaces V^h and V^h_T, from Eqs. (5) and (6), as our test and trial spaces, respectively. V^h is defined as the span of basis functions, such that any test function in V^h, for example $v^h \in V^h$, can be represented as a linear combination of the basis functions:

$$v^h(\boldsymbol{x}) = \sum_{i=1}^{N_{\text{dofs}}} \hat{\mathrm{v}}_i\, N_i(\boldsymbol{x}) = \hat{\mathbf{v}}^{\mathrm{T}}\mathbf{N}(\boldsymbol{x})\,. \tag{9}$$

Similarly, any trial function in V^h_T, for example $\phi^h \in V^h_T$, can be written as a linear combination of the basis functions with time-dependent weighting coefficients:

$$\phi^h(t,\boldsymbol{x}) = \sum_{i=1}^{N_{\text{dofs}}} \hat{\phi}_i(t)\, N_i(\boldsymbol{x}) = \hat{\boldsymbol{\phi}}^{\mathrm{T}}(t)\,\mathbf{N}(\boldsymbol{x}) \quad \text{with } \hat{\phi}_i(t) \in \mathcal{C}^\infty(0,T)\,. \tag{10}$$

In the following subsections, we provide a comprehensive overview of the individual components that comprise the mass and stiffness matrices of the semi-discrete formulation.

3.1.1. Neumann formulation

First, we consider a pure Neumann problem, i.e., $\partial\Omega = \partial\Omega_N$ and $\partial\Omega_D = \emptyset$. Then, for any $t \in (0, T)$, a finite element approximation produces the following semi-discrete formulation:

Find $\phi^h \in V^h_T$ s.t. $\forall\, v^h \in V^h$:

$$\int_\Omega \rho \frac{\mathrm{d}^2}{\mathrm{d}t^2}\phi^h v^h \,\mathrm{d}\Omega + \int_\Omega \kappa \nabla\phi^h \cdot \nabla v^h \,\mathrm{d}\Omega = \int_\Omega f\, v^h \,\mathrm{d}\Omega - \int_{\partial\Omega_N} g\, v^h \,\mathrm{d}S\,. \tag{11}$$

Substitution of the representation of ϕ^h and v^h from Eqs. (9) and (10) into Eq. (11) results in the following system of ordinary differential equations

$$\mathbf{M}\,\frac{\mathrm{d}^2}{\mathrm{d}t^2}\hat{\boldsymbol{\phi}} + \mathbf{K}\,\hat{\boldsymbol{\phi}} = \mathbf{F}\,, \tag{12}$$

with:

$$\big[\mathbf{M}\big]_{ij} = M\big(N_i(\boldsymbol{x}), N_j(\boldsymbol{x})\big) = \int_\Omega \rho N_i(\boldsymbol{x}) N_j(\boldsymbol{x}) \,\mathrm{d}\Omega\,, \tag{13a}$$

$$\big[\mathbf{K}\big]_{ij} = K\big(N_i(\boldsymbol{x}), N_j(\boldsymbol{x})\big) = \int_\Omega \kappa \nabla N_i(\boldsymbol{x}) \cdot \nabla N_j(\boldsymbol{x}) \,\mathrm{d}\Omega\,, \tag{13b}$$

$$\big[\mathbf{F}\big]_{i} = F\big(N_i(\boldsymbol{x})\big) = \int_\Omega f(\boldsymbol{x})\, N_i(\boldsymbol{x}) \,\mathrm{d}\Omega - \int_{\partial\Omega_N} g(\boldsymbol{x})\, N_i(\boldsymbol{x}) \,\mathrm{d}S\,. \tag{13c}$$

For this Neumann problem, the immersogeometric framework primarily impacts the selection of the discrete approximation space V^h as the span of non-boundary fitted B-spline basis functions, and the procedure for carrying out the integrals in Eq. (13).

3.1.2. Row-sum mass lumping

A fully-discrete formulation of Eq. (12) typically follows from a finite-difference type approximation to the time-derivative. When an explicit time-stepping scheme is adopted, such as a second-order Newmark-type central difference method or a higher-order explicit Runge–Kutta scheme, then the time-marching does not necessitate an inverse of the stiffness matrix. It does, however, require an inverse of the mass matrix. To avoid significant computational expense (both in terms of storage and operation count), the mass matrix is often manipulated to attain a diagonal matrix, which can be inverted trivially. This manipulation process is referred to as "mass lumping" and various methods exist, such as diagonal scaling [35], manifold-based methods [36] and lumping by nodal quadrature [37,38]. In this article, we focus on row-sum lumping, where the diagonal value is set to the sum-total of the row. This sum-total of the row corresponds to the multiplication of the row by a vector of ones. For a partition of unity basis, such as the employed B-spline basis, the vector of ones represents a field of unit value. Consequently, the lumped mass matrix can be written as:

$$\left[\mathbf{M}_D\right]_{ij} = \begin{cases} 0 & \text{if } i \neq j \\ M\big(1, N_i(\boldsymbol{x})\big) = \int_\Omega \rho N_i \,\mathrm{d}\Omega & \text{if } i = j \end{cases}. \tag{14}$$

Ensuring that the diagonal entries of $\mathbf{M}_D$ are positive is of crucial importance: negative components would cause negative eigenvalues, inducing exponential growth of the corresponding eigenmode. As pointed out in Section 2.1, the non-negativity property of the B-spline basis-functions guarantees positivity of $\int_\Omega N_i(x)\,\mathrm{d}\Omega$, and thus of the diagonal entries of $\mathbf{M}_D$, irrespective of how elements are cut. The same cannot be guaranteed for, for example, more classical $\mathcal{C}^0$-continuous Lagrange basis functions.

Remark 1. In the analysis in Sections 3.2 and 4.2 we require evaluations of the vector–matrix–vector product $\hat{\mathbf{v}}^{\mathrm{T}}\mathbf{M}_D\hat{\mathbf{v}}$ for various $\hat{\mathbf{v}}$. Unlike the consistent mass matrix (for which $\hat{\mathbf{v}}^{\mathrm{T}}\mathbf{M}\hat{\mathbf{v}} = \int_\Omega \rho\, v^h v^h \,\mathrm{d}\Omega$), the ad-hoc nature of the mass-lumping procedure implies that the operation $\hat{\mathbf{v}}^{\mathrm{T}}\mathbf{M}_D\hat{\mathbf{v}}$ does not permit an integral-based bilinear form. However, for those particular functions whose vector of coefficients ($\hat{\mathbf{v}}$ in Eq. (9)) exclusively consists of ones and zeros ($[\hat{\mathbf{v}}]_i \in \{0, 1\}$), the following integral evaluation of the vector–matrix–vector product is valid:

$$\hat{\mathbf{v}}^{\mathrm{T}}\mathbf{M}_D\hat{\mathbf{v}} = M\big(1, v^h(\boldsymbol{x})\big) = \int_\Omega \rho v^h(\boldsymbol{x})\,\mathrm{d}\Omega =: M_D\big(v^h(\boldsymbol{x})\big)\,. \tag{15}$$

3.1.3. Dirichlet condition enforcement by penalization

The remaining challenge in solving Eq. (8) in an immersed setting, is the imposition of Dirichlet boundary conditions. In Eq. (8), these are essential conditions, and they are imposed on the function space itself. For boundary-fitted methods, this can be mimicked by strongly prescribing nodal values. For immersed methods, however, the nodes are no longer placed on the domain boundary and the conventional procedure is not feasible. However, we can still integrate along this immersed boundary, as described in Section 2.2. Hence, boundary conditions can be incorporated weakly; through the addition of integral terms in the weak formulation targeted at enforcing the constraints.

The most common approach for weak imposition of Dirichlet conditions in explicit analysis is by penalty enforcement [5]:

$$\begin{aligned} &\text{Find } \phi^h \in V_T^h \text{ s.t. } \forall\, v^h \in V^h : \\ &M\Big(\frac{\mathrm{d}^2}{\mathrm{d}t^2}\phi^h, v^h\Big) + K(\phi^h, v^h) + \underbrace{\int_{\partial\Omega_D} \kappa\beta\, \phi^h\, v^h \,\mathrm{d}S}_{K_\beta\left(\phi^h, v^h\right)} = F(v^h) + \underbrace{\int_{\partial\Omega_D} \kappa\beta\, \phi_D\, v^h \,\mathrm{d}S}_{F_\beta\left(v^h\right)}, \end{aligned} \tag{16}$$

where $\beta > 0$. The additional contributions to the stiffness matrix and force vector read:

$$\left[\mathbf{K}_\beta\right]_{ij} = K_\beta\big(N_i(\boldsymbol{x}), N_j(\boldsymbol{x})\big) = \int_{\partial\Omega_D} \kappa\beta\, N_i(\boldsymbol{x}) N_j(\boldsymbol{x})\,\mathrm{d}S \tag{17a}$$

$$\left[\mathbf{F}_\beta\right]_i = F_\beta\big(N_i(\boldsymbol{x})\big) = \int_{\partial\Omega_D} \kappa\beta\,\phi_D(\boldsymbol{x}) N_i(\boldsymbol{x})\,\mathrm{d}S\,. \tag{17b}$$

To be dimensionally consistent, β^{-1} needs to have unit length. Suitable scaling of the eigenvalues associated to the penalty term is achieved when the penalty is chosen to scale inversely with the size of the elements of the background mesh h_K [5,39–41]:

$$\beta\big|_K = \bar{\beta}\, h_K^{-1}\,, \tag{18}$$

where $\bar{\beta}$ is a dimensionless global constant.

The penalty method offers a number of advantages, such as the absence of stringent restrictions on the penalty parameter to ensure positivity of eigenvalues, owing to the positive semi-definiteness of the contribution to the stiffness matrix, and its ease of implementation. A significant drawback is its variationally inconsistent nature (in the sense of [37]), which leads to a loss of optimal convergence rate that may result in error increases of orders of magnitude. The optimal convergence rate may be retrieved by choosing a penalty scaling stronger than h^{-1} [42] or by means of a projection-based penalty approach [43]. These are, however, not viable options in the context of explicit analysis, as the larger effective penalty value would soon increase the largest eigenvalue, and hence negatively affects the critical time-step size. Moreover, the solution quality is sensitive to the choice of penalty parameter, for which rigorous estimates are not available. Also in this regard, one must exercise caution not to choose the penalty values too large to avoid impacting the critical time-step size [5].

3.1.4. Dirichlet condition enforcement by Nitsche's method

The penalty method can be augmented by terms to make it variationally consistent, mitigating many of the just mentioned drawbacks. When this is done in a symmetric manner, this is called Nitsche's method [44]:

Find $\phi^h \in V_T^h$ s.t. $\forall\, v^h \in V^h$:

$$\begin{aligned} M\Big(\frac{\mathrm{d}^2}{\mathrm{d}t^2}\phi^h, v^h\Big) + K(\phi^h, v^h) + K_\beta(\phi^h, v^h) \underbrace{- \int_{\partial\Omega_D} \kappa\nabla\phi^h\cdot\boldsymbol{n}\, v^h\,\mathrm{d}S - \int_{\partial\Omega_D} \kappa\nabla v^h\cdot\boldsymbol{n}\,\phi^h\,\mathrm{d}S}_{K_{\mathrm{cs}}\left(\phi^h, v^h\right)} \\ = F(v^h) + F_\beta(v^h) \underbrace{- \int_{\partial\Omega_D} \kappa\phi_D\nabla v^h\cdot\boldsymbol{n}\,\mathrm{d}S}_{F_{\mathrm{s}}\left(v^h\right)}\,. \end{aligned} \tag{19}$$

The new matrix and vector contributions originating from the consistency and symmetry terms may be identified as:

$$\left[\mathbf{K}_{\mathrm{cs}}\right]_{ij} = K_{\mathrm{cs}}\big(N_i(\boldsymbol{x}), N_j(\boldsymbol{x})\big) = -\int_{\partial\Omega_D} \kappa\nabla N_i\cdot\boldsymbol{n}\, N_j\,\mathrm{d}S - \int_{\partial\Omega_D} \kappa\nabla N_j\cdot\boldsymbol{n}\, N_i\,\mathrm{d}S\,, \tag{20a}$$

$$\left[\mathbf{F}_{\mathrm{s}}\right]_i = F_{\mathrm{s}}\big(N_i(\boldsymbol{x})\big) = -\int_{\partial\Omega_D} \kappa\phi_D\,\nabla N_i\cdot\boldsymbol{n}\,\mathrm{d}S\,. \tag{20b}$$

Due to the added terms, the stiffness matrix is no-longer unconditionally positive definite. When β is chosen too small, the stiffness matrix may include negative eigenvalues. Negativity of eigenvalues carries over to the mass-to-stiffness generalized eigenvalue problem, again leading to detrimental exponential growth of the corresponding eigenmodes in time. The restriction on β to ensure positive definiteness has been studied extensively [45–47], and follows in each element K from a local inverse estimate. We make use of the following choice:

$$\beta\big|_K = 2\sup_{v^h\in V^h} \frac{\|\nabla v^h\cdot\boldsymbol{n}\|^2_{\partial\Omega_D\cap K}}{\|\nabla v^h\|^2_{\Omega\cap K}} \propto \frac{1}{h_c}\Big|_K\,, \tag{21}$$

where h_c is a length-scale associated to the cut element.

The element size for cut elements is not unambiguously defined. The inverse estimate in Eq. (21) can be bound by a size-independent factor multiplied by the ratio of the area of the Dirichlet surface to the volume of the cut-element [48,49]. This length parameter provides a suitable size measure for small-cut elements, however it does not limit to h_K for (nearly) uncut cases. In what follows, we make use of the following definition of h_c, which is consistent for both small and large cuts:

$$h_c\big|_K = \min\left\{ \frac{\int_{\Omega\cap K} \mathrm{d}\Omega}{\int_{\partial\Omega_D\cap K} \mathrm{d}S} \;,\; \left[\int_{\Omega\cap K} \mathrm{d}\Omega\right]^{\frac{1}{d}} \right\} =: \chi h_K \,. \tag{22}$$

The element size fraction χ that implicitly follows from this definition as $\chi = h_c/h_K$ represents the central quantity in our study on the cut-sensitivity of the largest eigenvalues later on. For sliver cuts, χ equates to the cut element volume fraction $\eta = \int_{\Omega\cap K} \mathrm{d}\Omega / \int_K \mathrm{d}\Omega$ (used in earlier analysis [18]), and for shape-regular cut elements they relate as $\chi \propto \eta^{\frac{1}{d}}$.

We define the constant of proportionality in Eq. (21) as $\bar{\beta}\big|_K$, such that, by definition, we can make use of the following expression for $\beta\big|_K$:

$$\beta\big|_K = \bar{\beta}\big|_K \,(\chi\, h_K)^{-1} \,. \tag{23}$$

3.1.5. Ghost-stabilized stiffness

For elements with vanishing support in the physical domain, the coefficient β required to ensure positive definiteness of the complete stiffness matrix can become arbitrarily large, as is reflected by the requirement in Eq. (21). For implicit and steady analysis, such a large penalty factor has negative consequences on the stability and conditioning of the ensuing system [49]. To mitigate this issue, the support of small-cut basis functions must be extended into the domain interior. Doing so strongly, for example by adopting weighted extended basis B-splines (WEB-splines) [50], or by performing cell aggregation [51], requires manipulation of the basis functions. If this is undesirable, then a potential alternative is the addition of "ghost-penalty" stabilization [23,24]:

Find $\phi^h \in V_T^h$ s.t. $\forall\, v^h \in V^h$:

$$\begin{aligned} M(\frac{\mathrm{d}^2}{\mathrm{d}t^2}\phi^h, v^h) + K(\phi^h, v^h) + K_\beta(\phi, v^h) + K_{\mathrm{cs}}(\phi, v^h) + \underbrace{\int_{\Gamma_g} \kappa\gamma_K \,[\![\partial_n^{k+1}\phi^h]\!][\![\partial_n^{k+1}\phi^h]\!]\,\mathrm{d}S}_{K_\gamma\left(\phi^h,\, v^h\right)} \\ = F(v^h) + F_\beta(v^h) + F_{\mathrm{cs}}(v^h)\,, \end{aligned} \tag{24}$$

where $\Gamma_g = \bigcup \mathcal{F}_{\mathrm{ghost}}$ is the union of the ghost faces from Eq. (3) and Fig. 2(c), $[\![\cdot]\!]$ is the jump operator, and ∂_n^{k+1} is the normal gradient of order $k+1$, with k the order of continuity of the B-spline basis functions. In a more general sense, $K_\gamma\left(\cdot,\cdot\right)$ should include jump-terms of the normal derivatives of order 1 until the polynomial order p. Since we only consider maximum order of continuity splines, for which $k = p-1$, all but the highest normal derivatives vanish on element interfaces. The contribution to the stiffness matrix is:

$$\left[\,\mathbf{K}_\gamma\,\right]_{ij} = K_\gamma\big(N_i(\boldsymbol{x}), N_j(\boldsymbol{x})\big) = \int_{\Gamma_g} \kappa\gamma_K \,[\![\partial_n^{k+1} N_i]\!][\![\partial_n^{k+1} N_j]\!]\,\mathrm{d}S \,. \tag{25}$$

The new penalty between the domain interior elements and the cut elements effectively adds a stiffness to the deflection of weakly supported degrees of freedom. More technically, the ghost-penalty term extends coercivity from the domain interior to the background mesh [52]. When the parameter γ_K is large enough and scales with h_K^{2p-1}, β is permitted to scale with the background-element size h_K rather than with the cut-element size $h_c = \chi\, h_K$:

$$\gamma_K\big|_K = \bar{\gamma}_K\, h_K^{2p-1} \,, \tag{26a}$$

$$\beta\big|_K = \bar{\beta}\, h_K^{-1} \,. \tag{26b}$$

The minimal permitted values of the pre-factors $\bar{\gamma}_K$ and $\bar{\beta}$ is still an open research question [52,53]. In the current work, we choose a sufficiently large $\bar{\gamma}_K$ to enable the use of a small $\bar{\beta}$, and experimentally verify that the ensuing stiffness matrix is positive definite.

3.1.6. Ghost-stabilized mass

The final ingredient that we choose to add to our explicit immersogeometric formulation is a "ghost-mass" term. We propose this term as a type of consistent mass scaling, with the intent of reducing the maximum eigenvalues that are caused by small-cut elements. The following additional component is introduced to the mass matrix [25,26,54]:

$$M_\gamma(\frac{\mathrm{d}^2}{\mathrm{d}t^2}\phi^h, v^h) = \int_{\Gamma_g} \rho\gamma_M \, [\![\partial_n^{k+1}\frac{\mathrm{d}^2}{\mathrm{d}t^2}\phi^h]\!][\![\partial_n^{k+1}\phi^h]\!] \, \mathrm{d}S \,, \tag{27}$$

$$\left[\mathbf{M}_\gamma\right]_{ij} = M_\gamma\big(N_i(\boldsymbol{x}), N_j(\boldsymbol{x})\big) \,. \tag{28}$$

If lower-order regularity B-splines are used, $M_\gamma(\cdot,\cdot)$ should include penalties on the jumps of all lower-order normal derivatives as well. These jumps vanish for the $\mathcal{C}^{p-1}$-continuous B-splines considered herein.

The ghost-mass term adds inertia to the acceleration of the deflection of the weakly supported degrees of freedom. As $\mathbf{M}_\gamma$ represents a positive semi-definite contribution to the mass matrix, it serves to reduce the eigenvalues of modes that excite the $M_\gamma(\cdot,\cdot)$ term, i.e., those with derivative changes across boundaries of elements with small interior support. At the same time, the term is consistent for sufficiently smooth solutions, such that it does not introduce a modeling error. In particular, the term does not adversely affect the modes and frequencies at the low-frequency range of the spectrum that originates from the mass-to-stiffness generalized eigenvalue problem [25,26].

The required scaling of the penalty parameter γ_M is different than that of γ_K in the stiffness matrix, as already follows from a dimensional consistency argument. We make use of the following scaling:

$$\gamma_M = \bar{\gamma}_M \, h_K^{2p+1} \,. \tag{29}$$

where the appropriate choice of $\bar{\gamma}_M$ is investigated in Section 3.2.

Remark 2. The matrix that follows from the ghost-mass term is not amendable to standard row-sum lumping. Recall from Section 3.1.2 that the row-sum represents the action of the corresponding bilinear form on a field of unit value, and, as can be observed from Eq. (27), $M_\gamma(1, v^h) = 0$. When the immersed boundary elements make up a relatively small portion of the mesh, the computational expense involved in inverting the mass matrix may not cause a bottleneck (especially when the LU-factorization is stored and reused). Nevertheless, various strategies could be considered to efficiently approximate an inverse to the scaled mass matrix. One could reduce the number of ghost faces in such a way that $\mathbf{M}_\gamma$ becomes block-diagonal [55], or approximate the inverse in a (block) Jacobi sense, or attempt row-sum lumping of the absolute values of the matrix components, or consider different classes of discrete extension operators altogether [56]. However, since the primary focus of this work is the analysis of the explicit immersogeometric formulations, we consider the development of such optimized implementation strategies beyond the scope of this article, and we exclusively consider $\mathbf{M}_\gamma$ in its full form.

3.2. Analysis of the critical time-step size

The various stiffness terms proposed in the previous section can be collected in the total stiffness bilinear form $\tilde{K}(\cdot,\cdot)$, to produce the total stiffness matrix $\tilde{\mathbf{K}}$. Similarly, the total inertial bilinear form $\tilde{M}(\cdot,\cdot)$ and mass matrix $\tilde{\mathbf{M}}$ follow from the chosen combination of a consistent or lumped mass matrix, and potentially a ghost-mass contribution. The general semi-discrete form then reads:

$$\begin{aligned} &\text{Find } \phi^h \in V_T^h \text{ s.t. } \forall\, v^h \in V^h : \\ &\quad \tilde{M}(\tfrac{\mathrm{d}^2}{\mathrm{d}t^2}\phi^h, v^h) + \tilde{K}(\phi^h, v^h) = \tilde{F}(v^h) \,, \end{aligned} \qquad \Leftrightarrow \qquad \tilde{\mathbf{M}}\,\frac{\mathrm{d}^2}{\mathrm{d}t^2}\hat{\boldsymbol{\phi}} + \tilde{\mathbf{K}}\,\hat{\boldsymbol{\phi}} = \tilde{\mathbf{F}} \,. \tag{30}$$

As addressed in the introduction, the critical time-step size of an explicit time-stepping treatment of Eq. (30) is inversely related to the maximum eigenvalue of the generalized eigenvalue problem:

$$\tilde{K}(\xi^h, v^h) = \lambda \tilde{M}(\xi^h, v^h) \quad \forall\, v^h \in V^h \qquad \Leftrightarrow \qquad \tilde{\mathbf{K}}\,\hat{\boldsymbol{\xi}} = \lambda \tilde{\mathbf{M}}\,\hat{\boldsymbol{\xi}} \,. \tag{31}$$

For symmetric matrices, the maximum eigenvalue is the largest value of the generalized Rayleigh quotient:

$$\lambda_{\max} \geq \mathcal{R}(\tilde{\mathbf{K}}, \tilde{\mathbf{M}}, \hat{\boldsymbol{\xi}}) = \frac{\hat{\boldsymbol{\xi}}^{\mathrm{T}}\tilde{\mathbf{K}}\,\hat{\boldsymbol{\xi}}}{\hat{\boldsymbol{\xi}}^{\mathrm{T}}\tilde{\mathbf{M}}\,\hat{\boldsymbol{\xi}}} = \frac{\tilde{K}(\xi^h, \xi^h)}{\tilde{M}(\xi^h, \xi^h)} \qquad \forall\, \hat{\boldsymbol{\xi}} \in \mathbb{R}^N \,,\ \xi^h = \sum_{n=0}^{N} \hat{\boldsymbol{\xi}}_n N_n(\boldsymbol{x}) \,, \tag{32}$$

where the equality holds for $\hat{\boldsymbol{\xi}} = \hat{\boldsymbol{\xi}}_{\max}$. Due to the bilinearity of the forms, the various components separate into individual contributions:

$$\mathcal{R}(\tilde{\mathbf{K}}, \tilde{\mathbf{M}}, \hat{\boldsymbol{\xi}}) = \frac{K(\xi,\xi) + K_{\mathrm{cs}}(\xi,\xi) + K_{\beta}(\xi,\xi) + K_{\gamma}(\xi,\xi)}{M(\xi,\xi) + M_{\gamma}(\xi,\xi)}\,. \tag{33}$$

We now wish to analyze whether $\lambda_{\max}$, and by induction, the critical time-step size, is sensitive to the size and shape of the cut elements, as characterized by the parameter χ in Eq. (22). For $\chi \to 0$, the generalized Rayleigh quotient approaches the ratio of the lowest-order scaling of each of the components in the numerator divided by the lowest-order scaling of each of the components in the denominator. For some $\hat{\boldsymbol{\xi}}$, we can then characterize the scaling of the generalized Rayleigh quotient as:

$$\mathcal{R}(\mathbf{K}, \mathbf{M}, \hat{\boldsymbol{\xi}}) = \mathcal{O}\big(\chi^{q}\big)\,. \tag{34}$$

If there exists any $\hat{\boldsymbol{\xi}}$ such that $q < 0$, then, by Eq. (32), the maximum eigenvalue can become arbitrarily large for arbitrarily small cuts, resulting in an unfeasibly small critical time-step size. Those $\hat{\boldsymbol{\xi}}$ for which $q = 0$ cause cut-*shape* dependent eigenvalues that may turn out to be dominant. Those corresponding to $q > 0$ are suppressed as the cut becomes small.

Our study on the impact of the cut elements on the time-step estimate thus revolves around the examination of the generalized Rayleigh quotient for selected examples of problematic cut cases. In this regard, we consider two distinct types of cuts: corner cuts and sliver cuts. These are two extreme cases that may arise even when the background mesh is sufficiently refined to resolve small-scale geometric features. On these cut elements, we consider two different functions: one predominantly supported in the domain interior and one predominantly supported in the domain exterior. All four functions are depicted for the example of a two-dimensional domain in Fig. 5(a) to Fig. 5(d). In one dimension, the four cases reduce to the two functions plotted in Figs. 5(e) and 5(f). For all functions considered, the coefficient vector consists exclusively of ones and zeros, whereby the condition of Remark 1 is satisfied, and $\hat{\boldsymbol{\xi}}^{\mathrm{T}}\mathbf{M}_D\hat{\boldsymbol{\xi}}$ may be evaluated as $M_D(\xi)$.

We determine the generalized Rayleigh quotient for different collections of components to the mass and stiffness matrix, i.e., for different finite element formulations. For the stiffness matrix, we consider a pure Neumann boundary, a pure penalty method with $\beta = \bar{\beta}h_K^{-1}$, Nitsche's method with $\beta = \bar{\beta}h_c^{-1} = \bar{\beta}(\chi\, h_K)^{-1}$, and Nitsche's method combined with a ghost-penalty term and the choices $\beta = \bar{\beta}h_K^{-1}$ and $\gamma_K = \bar{\gamma}_K h_K^{2p-1}$. For the mass matrix, we consider the consistent mass matrix of Eq. (13a), a consistent mass matrix with ghost stabilization with $\gamma_M = \bar{\gamma}_M h_K^{2p+1}$, a lumped mass matrix per Eq. (14), and a lumped mass matrix with (non-lumped) ghost stabilization.

Carrying out all the generalized Rayleigh quotients computations for the corner-cut functions of Figs. 5(a) and 5(b) results in the scalings detailed in Tables 1 and 2, respectively, and for the sliver functions depicted in Figs. 5(c) and 5(d) results in Tables 3 and 4, respectively. Cells in the tables marked in red indicate formulations and cut-cases for which the generalized Rayleigh quotient increases for decreasing cut-size, i.e., for $\chi \to +0$. Green cells signify formulations and cut-cases for which the generalized Rayleigh quotient decreases for decreasing cut-size, representing stable cases. The beige and yellow cells denote conditionally stable cases: there are restrictions on the polynomial order, spatial dimension and/or the penalty parameter for which the generalized Rayleigh quotient may or may not dominate and/or increase with decreasing cut-size.

Table 5 provides a comprehensive summary of findings that follow from the scaling relations detailed in Tables 1–4. The following conclusions stand out:

- The first column of Table 5 is fully colored red, expressing that the use of a consistent mass matrix without a form of mass scaling is not applicable for explicit immersed computation. A consistent mass matrix is unconventional for explicit analysis due to the implied cost of inversion, but in an immersed setting the largest eigenvalue may also become arbitrarily large for small cut elements, causing unfeasibly small critical time-step sizes.
- The light-red coloring of the first two rows of the second column in Table 5 indicates that lumping the mass matrix can mitigate the problematic cut-size dependent scaling of the maximum eigenvalue, but only when the polynomial order of the basis function is at least quadratic. This was first observed in [21].
- To enable the use of linear basis functions, ghost-stabilized mass must be added to ensure that the critical time-step sizes remain independent of the cut-size. This formulation corresponds to the last column in Table 5, which is the only column with green cells.

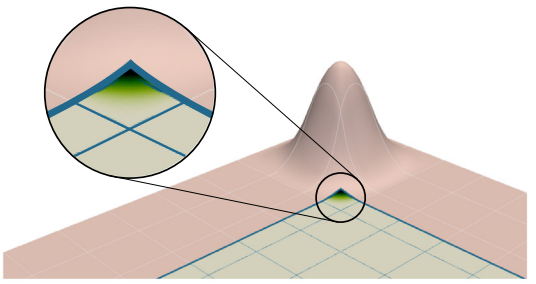

(a) First corner-cut function, $\hat{\boldsymbol{\xi}} = \left[\cdots 0, 1, 0, \cdots\right]^{\mathrm{T}}$.

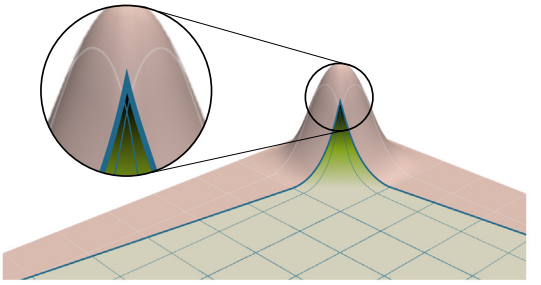

(b) Second corner-cut function, $\hat{\boldsymbol{\xi}} = \left[\cdots 0, 1, 0, \cdots\right]^{\mathrm{T}}$.

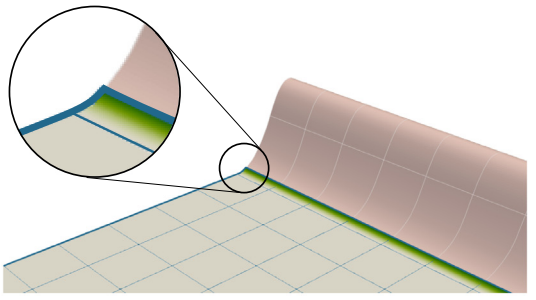

(c) First sliver-cut function, $\hat{\boldsymbol{\xi}} = \left[\cdots 0, 1, 1, \cdots 1, 1, 0, \cdots\right]^{\mathrm{T}}$.

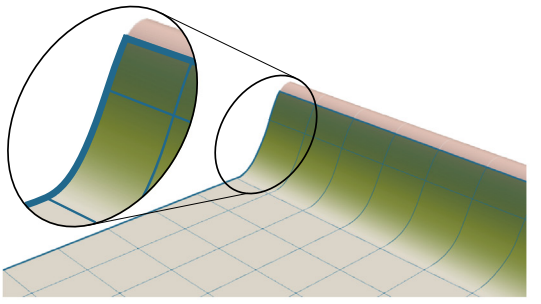

(d) Second sliver-cut function, $\hat{\boldsymbol{\xi}} = \left[\cdots 0, 1, 1, \cdots 1, 1, 0, \cdots\right]^{\mathrm{T}}$.

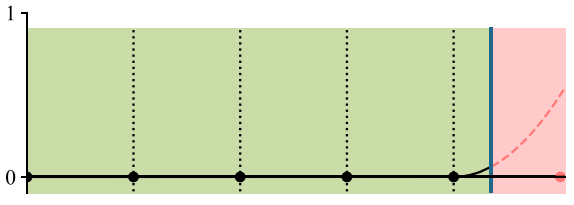

(e) First cut function in one dimension, $\hat{\boldsymbol{\xi}} = \left[\cdots 0, 1, 0, \cdots\right]^{\mathrm{T}}$.

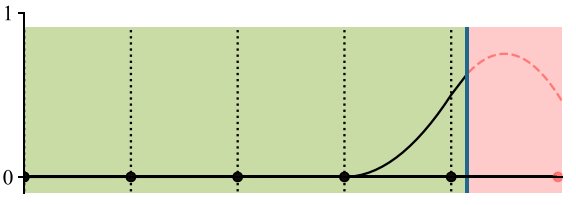

(f) Second cut function in one dimension, $\hat{\boldsymbol{\xi}} = \left[\cdots 0, 1, 0, \cdots\right]^{\mathrm{T}}$.

Fig. 5. Functions under consideration for cut-size scaling. Green represents the domain interior and red the domain exterior.

- When a penalty method is used for the enforcement of Dirichlet constraints, the maximum eigenvalue scales linearly with the non-dimensionalized penalty parameter $\bar{\beta}$, as is indicated by the light-red and beige cells in the second row of Table 5. This is a known issue [5], and this undesirable scaling cannot be fixed by adding a ghost-mass term, nor by raising the polynomial order.
- A Nitsche formulation with local penalty parameter (i.e., without the ghost-stiffness term) does not yield a cut-size independent critical time-step size. The resulting scaling reminds of the degenerative error bounds due to sliver cuts proven in [49].
- To adopt Nitsche's method in a stable manner, one requires both a ghost-mass term and a ghost-stiffness term. Both penalty terms must scale with the uncut-element size h_K. To keep the maximum eigenvalue small, the ghost-mass penalty $\bar{\gamma}_M$ must be of the same order of magnitude as the ghost-stiffness penalty $\bar{\gamma}_K$, and the Nitsche penalty $\bar{\beta}$ must be as small as possible. In contrast to a penalty method, using a small $\bar{\beta}$ does not adversely impact solution quality, and hence we color this bottom-right box green.

Table 1
Resulting scaling with cut size for the first corner-cut function for the second-order problem.

		Consistent mass (Eq. (13a))	Lumped mass (Eq. (14))	Consistent/lumped mass and ghost mass (Eq. (28)) with $\gamma_M = \bar{\gamma}_M h^{2p+1}$
	$\mathcal{O}(\tilde{M})$ / $\mathcal{O}(\tilde{K})$	χ^{2pd+d}	χ^{pd+d}	$\bar{\gamma}_M \chi^0$
Neumann (Eq. (11))	$\chi^{2pd+d-2}$	χ^{-2}	* χ^{pd-2}	$\bar{\gamma}_M^{-1}\chi^{2pd+d-2}$
Penalty (Eq. (16)) with $\beta = \bar{\beta}h_K^{-1}$	$\chi^{2pd+d-2}$	χ^{-2}	* χ^{pd-2}	$\bar{\gamma}_M^{-1}\chi^{2pd+d-2}$
Nitsche (Eq. (19)) with $\beta = \bar{\beta}(\chi h_K)^{-1}$	$\bar{\beta}\chi^{2pd+d-2}$	$\bar{\beta}\chi^{-2}$	** $\bar{\beta}\chi^{pd-2}$	$\bar{\beta}\bar{\gamma}_M^{-1}\chi^{2pd+d-2}$
Nitsche and ghost (Eq. (24)) $\beta = \bar{\beta}h_K^{-1}$, $\gamma_K = \bar{\gamma}_K h^{2p-1}$	$\bar{\gamma}_K\chi^0$	$\bar{\gamma}_K\chi^{-2pd-d}$	$\bar{\gamma}_K\chi^{-pd-d}$	$\bar{\gamma}_K\bar{\gamma}_M^{-1}\chi^0$

*: Unstable for $d = 1$ and $p = 1$.
**: Unstable for $d = 1$ and $p = 1$, and may dominate for $d = 2$ and $p = 1$.

Table 2
Resulting scaling with cut size for the second corner-cut function for the second-order problem.

		Consistent mass (Eq. (13a))	Lumped mass (Eq. (14))	Consistent/lumped mass and ghost mass (Eq. (28)) with $\gamma_M = \bar{\gamma}_M h^{2p+1}$
	$\mathcal{O}(\tilde{M})$ / $\mathcal{O}(\tilde{K})$	χ^0	χ^0	χ^0
Neumann (Eq. (11))	χ^0	χ^0	χ^0	χ^0
Penalty (Eq. (16)) with $\beta = \bar{\beta}h_K^{-1}$	$\bar{\beta}\chi^0$	* $\bar{\beta}\chi^0$	* $\bar{\beta}\chi^0$	* $\bar{\beta}\chi^0$
Nitsche (Eq. (19)) with $\beta = \bar{\beta}(\chi h_K)^{-1}$	$\bar{\beta}\chi^{d-2}$	** $\bar{\beta}\chi^{d-2}$	** $\bar{\beta}\chi^{d-2}$	** $\bar{\beta}\chi^{d-2}$
Nitsche and ghost (Eq. (24)) $\beta = \bar{\beta}h_K^{-1}$, $\gamma_K = \bar{\gamma}_K h^{2p-1}$	$\bar{\beta}\chi^0$	*** $\bar{\beta}\chi^0$	*** $\bar{\beta}\chi^0$	*** $\bar{\beta}\chi^0$

*: Adverse scaling with $\bar{\beta}$.
**: Unstable for $d = 1$.
***: Adverse scaling with $\bar{\beta}$, but only small $\bar{\beta}$ is required for sufficient accuracy.

Table 3
Resulting scaling with cut size for the first sliver-cut function for the second-order problem.

		Consistent mass (Eq. (13a))	Lumped mass (Eq. (14))	Consistent/lumped mass and ghost mass (Eq. (28)) with $\gamma_M = \bar{\gamma}_M h^{2p+1}$
	$\mathcal{O}(\tilde{M})$ / $\mathcal{O}(\tilde{K})$	χ^{2p+1}	χ^{p+1}	$\bar{\gamma}_M \chi^0$
Neumann (Eq. (11))	χ^{2p-1}	χ^{-2}	χ^{p-2}	$\bar{\gamma}_M^{-1}\chi^{2p-1}$
Penalty (Eq. (16)) with $\beta = \bar{\beta}h_K^{-1}$	χ^{2p-1}	χ^{-2}	χ^{p-2}	$\bar{\gamma}_M^{-1}\chi^{2p-1}$
Nitsche (Eq. (19)) with $\beta = \bar{\beta}(\chi h_K)^{-1}$	$\bar{\beta}\chi^{2p-1}$	$\bar{\beta}\chi^{-2}$	$\bar{\beta}\chi^{p-2}$	$\bar{\beta}\bar{\gamma}_M^{-1}\chi^{2p-1}$
Nitsche and ghost (Eq. (24)) $\beta = \bar{\beta}h_K^{-1}$, $\gamma_K = \bar{\gamma}_K h^{2p-1}$	$\bar{\gamma}_K\chi^0$	$\bar{\gamma}_K\chi^{-2p-1}$	$\bar{\gamma}_K\chi^{-p-1}$	$\bar{\gamma}_K\bar{\gamma}_M^{-1}\chi^0$

Table 4
Resulting scaling with cut size for the second sliver-cut function for the second-order problem.

		Consistent mass (Eq. (13a))	Lumped mass (Eq. (14))	Consistent/lumped mass and ghost mass (Eq. (28)) with $\gamma_M = \bar{\gamma}_M h^{2p+1}$
	$\diagdown \mathcal{O}(\tilde{M})$ $\mathcal{O}(\tilde{K}) \diagdown$	χ^0	χ^0	χ^0
Neumann (Eq. (11))	χ^0	χ^0	χ^0	χ^0
Penalty (Eq. (16)) with $\beta = \bar{\beta} h_K^{-1}$	$\bar{\beta}\chi^0$	* $\bar{\beta}\chi^0$	* $\bar{\beta}\chi^0$	* $\bar{\beta}\chi^0$
Nitsche (Eq. (19)) with $\beta = \bar{\beta}(\chi h_K)^{-1}$	$\bar{\beta}\chi^{-1}$	$\bar{\beta}\chi^{-1}$	$\bar{\beta}\chi^{-1}$	$\bar{\beta}\chi^{-1}$
Nitsche and ghost (Eq. (24)) $\beta = \bar{\beta} h_K^{-1}$, $\gamma_K = \bar{\gamma}_K h^{2p-1}$	$\bar{\beta}\chi^0$	** $\bar{\beta}\chi^0$	** $\bar{\beta}\chi^0$	** $\bar{\beta}\chi^0$

*: Adverse scaling with $\bar{\beta}$.
**: Adverse scaling with $\bar{\beta}$, but only small $\bar{\beta}$ is required for sufficient accuracy.

Table 5
Overview of the stability characteristics for the second-order problem. Worst-case scaling of the cut scenarios considered in Tables 1–4.

	Consistent mass (Eq. (13a))	Lumped mass (Eq. (14))	Consistent/lumped mass and ghost mass (Eq. (28)) with $\gamma_M = \bar{\gamma}_M h^{2p+1}$
Neumann (Eq. (11))		Unstable for $p = 1$	Unnecessary for $p \geq 2$
Penalty (Eq. (16)) with $\beta = \bar{\beta} h_K^{-1}$		Unstable for $p = 1$ Scales with $\bar{\beta}$	Scales with $\bar{\beta}$
Nitsche (Eq. (19)) with $\beta = \bar{\beta}(\chi h_K)^{-1}$			
Nitsche and ghost (Eq. (24)) $\beta = \bar{\beta} h_K^{-1}$, $\gamma_K = \bar{\gamma}_K h^{2p-1}$			Requires $\bar{\gamma}_M \sim \bar{\gamma}_K$ and small $\bar{\beta}$

Remark 3. The utilization of maximum regularity B-spline basis functions in the analysis reduces the number of cut functions that need to be considered. As demonstrated in the subfigures of the left column of Fig. 3, all basis functions are identical up to affine transformation. The adoption of lower-order continuous basis functions, such as the C^0-continuous functions depicted in Figs. 3(b), 3(f) and 3(h), necessitates the examination of a more extensive collection of cut functions. In particular, as $\chi \to +0$, the C^0-continuous B-spline basis functions with small support locally approach lower-order polynomial functions, as is illustrated in Fig. 6. The lower-order polynomial functions are the critical cases in the first three rows of the middle column in Tables 1 and 4. For lower-order continuous B-splines, the polynomial order in those scaling relations should thus be replaced by $k + 1$, with k the order of continuity. This corroborates the conclusion from [21] that a sufficiently high regularity is required to mitigate the cut-size dependency of the critical time-step size.

Remark 4. The scaling relations documented in Tables 3 and 4 are precisely those of Tables 1 and 2, with $d = 1$. This concurrence is anticipated, as the cut functions depicted in Figs. 5(c) and 5(d) are effectively one-dimensional. Thus, for an arbitrary d-dimensional domain, one only needs to determine the scaling relations for the d-dimensional cut functions (e.g., those in Figs. 5(a) and 5(b)), and the scaling relations for the lower-dimensional cut functions can then be deduced by successively replacing d by the positive lower integer values below d.

4. Critical time-step analysis for a fourth-order problem

While the wave equation studied in the previous section is a prototypical model equation for explicit analysis, its second-order nature limits the relevance of the conclusions from Section 3.2 when considering higher-order

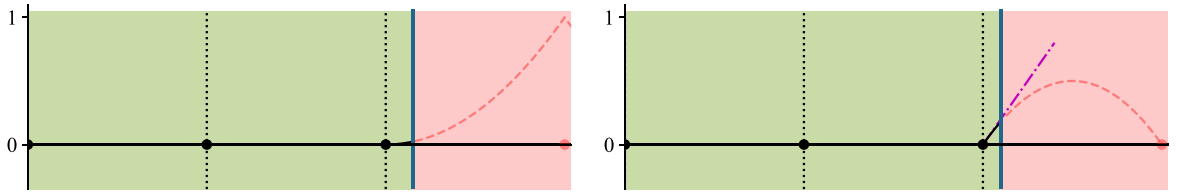

(a) A regular cut $p = 2$ basis function.

(b) A $p = 2$ cut basis function that approaches a cut $p = 1$ function as $\chi \to +0$.

Fig. 6. Cut basis functions for a quadratic $\mathcal{C}^0$-continuous B-spline.

formulations, such as shell formulations. To understand how the conclusions translate, we repeat the analysis of Section 3 in brief for the following fourth-order problem:

$$\rho \frac{\partial^2}{\partial t^2}\phi + \Delta(\kappa \Delta \phi) = f \qquad \text{in } \Omega \times (0,T) \subset \mathbb{R}^d \times [0,T]\,, \tag{35a}$$

$$\nabla(\kappa \Delta \phi) \cdot \boldsymbol{n} = q \qquad \text{on } \partial\Omega_q \times (0,T)\,, \tag{35b}$$

$$-\kappa \Delta \phi = m \qquad \text{on } \partial\Omega_m \times (0,T)\,, \tag{35c}$$

$$\nabla \phi \cdot \boldsymbol{n} = g \qquad \text{on } \partial\Omega_N \times (0,T)\,, \tag{35d}$$

$$\phi = \phi_D \qquad \text{on } \partial\Omega_D \times (0,T)\,, \tag{35e}$$

$$\phi = \phi_0 \qquad \text{on } \Omega \times \{0\}\,, \tag{35f}$$

$$\frac{\partial}{\partial t}\phi = \dot{\phi}_0 \qquad \text{on } \Omega \times \{0\}\,. \tag{35g}$$

This equation describes the bending of an Euler–Bernoulli beam in one spatial dimension and is a shell-type analog in two dimensions [57,58]. Eqs. (35d) and (35e) are essential boundary conditions, describing displacement and rotation at the edge, respectively. Eqs. (35b) and (35c) are natural conditions. A more direct link to shell formulations requires different forms of the natural boundary conditions, to represent the applied bending moment and shear force [58,59], but the expressions of Eqs. (35b) and (35c) are applicable for arbitrary spatial dimension, making them more suitable for a general time-step stability analysis. Note that, due to the fourth-order parabolic nature of the PDE, two boundary conditions must be prescribed at any location on the boundary.

4.1. Semi-discrete formulation

The weak formulation for the fourth-order problem of Eq. (35) reads:

$$\text{For a.e. } t \in (0,T), \text{ find } \phi \in H^2_{\phi_D,g}(\Omega) \text{ and } \frac{\partial^2}{\partial t^2}\phi \in H^{-2}(\Omega) \text{ s.t. } \forall\, v \in H^2_{0,0}(\Omega):$$

$$\begin{cases} \left\langle \dfrac{\partial^2}{\partial t^2}\phi,\, \rho v \right\rangle + \displaystyle\int_\Omega \kappa \Delta\phi\, \Delta v \,\mathrm{d}\Omega = -\int_{\partial\Omega_q} q\, v \,\mathrm{d}S - \int_{\partial\Omega_m} m\, \nabla v \cdot \boldsymbol{n} \,\mathrm{d}S\,, \\ \phi\big|_{t=0} = \phi_0\,, \\ \dfrac{\partial}{\partial t}\phi\Big|_{t=0} = \dot{\phi}_0\,, \end{cases} \tag{36}$$

with $H^2_{\phi_D,g}(\Omega)$ the $H^2(\Omega)$ Sobolev space for which each member satisfies the trace equalities from Eqs. (35d) and (35e), $H^{-2}(\Omega)$ is the corresponding dual space, and $\langle \cdot, \cdot \rangle$ denotes the pairing between them. If $\frac{\partial^2}{\partial t^2}\phi \in L^2(\Omega)$, then $\left\langle \frac{\partial^2}{\partial t^2}\phi,\, \rho v \right\rangle = \int_\Omega \rho \frac{\partial^2}{\partial t^2}\phi\, v \,\mathrm{d}\Omega$.

In an immersed setting, both essential constraints need to be enforced weakly. A semi-discrete formulation may again be written in the general form of:

$$\tilde{\mathbf{M}} \frac{\mathrm{d}^2}{\mathrm{d}t^2}\hat{\boldsymbol{\phi}} + \tilde{\mathbf{K}}\hat{\boldsymbol{\phi}} = \tilde{\mathbf{F}}\,, \tag{37}$$

where, as in the second-order case, the mass matrix may or may not be lumped and may or may not contain a ghost-penalty term. The stiffness matrix, in its most generic form, consists of the following terms:

$$\begin{aligned}\left[\mathbf{K}\right]_{ij} = &\int_{\Omega} \kappa\, \Delta N_i\, \Delta N_j \,\mathrm{d}\Omega + \int_{\Gamma_g} \kappa\gamma_K \left[\!\left[\partial_n^{k+1} N_i\right]\!\right]\left[\!\left[\partial_n^{k+1} N_j\right]\!\right] \mathrm{d}S \\ &+ \int_{\partial\Omega_D} \kappa\beta_\phi\, N_i N_j \,\mathrm{d}S + \int_{\partial\Omega_N} \kappa\beta_g\, \nabla N_i \cdot \boldsymbol{n}\, \nabla N_j \cdot \boldsymbol{n} \,\mathrm{d}S \\ &+ \int_{\partial\Omega_D} \nabla\big(\kappa\, \Delta N_i\big) \cdot \boldsymbol{n}\, N_j \,\mathrm{d}S + \int_{\partial\Omega_D} \nabla\big(\kappa\, \Delta N_j\big) \cdot \boldsymbol{n}\, N_i \,\mathrm{d}S \\ &- \int_{\partial\Omega_N} \nabla N_j \cdot \boldsymbol{n}\, \kappa\, \Delta N_i \,\mathrm{d}S - \int_{\partial\Omega_N} \nabla N_i \cdot \boldsymbol{n}\, \kappa\, \Delta N_j \,\mathrm{d}S\,.\end{aligned} \tag{38}$$

The second term is the ghost-penalty term, the third and fourth term are penalty terms for the enforcement of the two essential boundary conditions, and the last four terms are the consistency and symmetry terms to complete the Nitsche formulations.

For the penalty formulation, the following parameter scalings are applicable:

$$\beta_\phi\big|_K = \bar{\beta}_\phi h_K^{-3}\,, \tag{39a}$$

$$\beta_g\big|_K = \bar{\beta}_g h_K^{-1}\,. \tag{39b}$$

For the Nitsche formulation without ghost-penalty stabilization on the stiffness matrix, the positive definiteness (coercivity) requirement necessitates a minimum penalty value. We make use of:

$$\beta_\phi\big|_K = 3 \sup_{v^h \in V^h} \frac{\|\nabla(\Delta v^h)\cdot\boldsymbol{n}\|^2_{\partial\Omega_D\cap K}}{\|\Delta v^h\|^2_{\Omega\cap K}} =: \bar{\beta}_\phi\big|_K (\chi\, h_K)^{-3}\,, \tag{40a}$$

$$\beta_g\big|_K = 3 \sup_{v^h \in V^h} \frac{\|\Delta v^h\|^2_{\partial\Omega_N\cap K}}{\|\Delta v^h\|^2_{\Omega\cap K}} =: \bar{\beta}_g\big|_K (\chi\, h_K)^{-1}\,. \tag{40b}$$

When the stiffness matrix includes ghost-penalty stabilization, then we use the following parameters scalings, which satisfy the dimensional consistency requirement:

$$\gamma_K\big|_K = \bar{\gamma}\, h_K^{2p-3} \tag{41a}$$

$$\beta_\phi\big|_K = \bar{\beta}_\phi h_K^{-3}\,, \tag{41b}$$

$$\beta_g\big|_K = \bar{\beta}_g h_K^{-1}\,. \tag{41c}$$

4.2. Analysis of the critical time-step size

By following the methodology outlined in Section 3.2, we derive the scaling relations for the four cut functions depicted in Fig. 5. The results for the various formulations are collected in Tables 6 and 7 for the two corner-cut functions, and in Tables 8 and 9 for the two sliver-cut functions. The results for all four cut cases are combined and summarized in Table 10. The main conclusions drawn for the second-order equation carry over to this fourth-order problem:

- The use of a consistent mass matrix without mass scaling results in an undesirable cut-size dependent critical time-step size for all formulations.
- Lumping the mass matrix is insufficient to yield a cut-size independent scheme for spline basis functions of order $p = 2$ or even $p = 3$. To ensure a cut-size independent critical time-step size, either $p = 4$ basis function need to be used or ghost-stabilized mass needs to be added.
- For both penalty formulations, the maximum eigenvalue scales linearly with the non-dimensionalized penalty parameter $\bar{\beta}$, irrespective of the order of the basis functions and/or the use of mass scaling.
- Both Nitsche formulations with local penalty parameters (i.e., without a ghost-stiffness term) are inapplicable.
- Both Nitsche formulations require a ghost-mass term as well as a ghost-stiffness term to ensure a cut-size independent critical time-step size.

Table 6
Resulting scaling with cut size for the first corner-cut function for the fourth-order problem.

		Consistent mass (Eq. (13a))	Lumped mass (Eq. (14))	Consistent/lumped mass and ghost mass (Eq. (28)) with $\gamma_M = \bar{\gamma}_M h^{2p+1}$
	$\mathcal{O}(\tilde{M})$ / $\mathcal{O}(\tilde{K})$	χ^{2pd+d}	χ^{pd+d}	$\bar{\gamma}_M \chi^0$
Neumann	$\chi^{2pd+d-4}$	χ^{-4}	* χ^{pd-4}	$\bar{\gamma}_M^{-1}\chi^{2pd+d-4}$
Penalty on ϕ $\beta_\phi = \bar{\beta}_\phi h_K^{-3}$	$\chi^{2pd+d-4}$	χ^{-4}	* χ^{pd-4}	$\bar{\gamma}_M^{-1}\chi^{2pd+d-4}$
Nitsche on ϕ $\beta_\phi = \bar{\beta}_\phi(\chi h_K)^{-3}$	$\bar{\beta}_\phi\chi^{2pd+d-4}$	$\bar{\beta}_\phi\chi^{-4}$	* $\bar{\beta}_\phi\chi^{pd-4}$	$\bar{\beta}_\phi\bar{\gamma}_M^{-1}\chi^{2pd+d-4}$
Penalty on $\nabla\phi\cdot\boldsymbol{n}$ $\beta_g = \bar{\beta}_g h_K^{-1}$	$\chi^{2pd+d-4}$	χ^{-4}	* χ^{pd-4}	$\bar{\gamma}_M^{-1}\chi^{2pd+d-4}$
Nitsche on $\nabla\phi\cdot\boldsymbol{n}$ $\beta_g = \bar{\beta}_g(\chi h_K)^{-1}$	$\bar{\beta}_g\chi^{2pd+d-4}$	$\bar{\beta}_g\chi^{-4}$	* $\bar{\beta}_g\chi^{pd-4}$	$\bar{\beta}_g\bar{\gamma}_M^{-1}\chi^{2pd+d-4}$
Nitsche on ϕ, $\beta_\phi = \bar{\beta}_\phi h_K^{-3}$ on $\nabla\phi\cdot\boldsymbol{n}$, $\beta_g = \bar{\beta}_g(\chi h_K)^{-1}$ and ghost $\gamma_K = \bar{\gamma}_K h^{2p-1}$	$\bar{\gamma}_K\chi^0$	$\bar{\gamma}_K\chi^{-2pd-d}$	$\bar{\gamma}_K\chi^{-pd-d}$	$\bar{\gamma}_K\bar{\gamma}_M^{-1}\chi^0$

*: Unstable for $d = 1$ and $p = 2$.
**: Unstable for $d = 1$ and $p = 2$, and may dominate for $d = 2$ and $p = 2$.

Table 7
Resulting scaling with cut size for the second corner-cut function for the fourth-order problem.

		Consistent mass (Eq. (13a))	Lumped mass (Eq. (14))	Consistent/lumped mass and ghost mass (Eq. (28)) with $\gamma_M = \bar{\gamma}_M h^{2p+1}$
	$\mathcal{O}(\tilde{M})$ / $\mathcal{O}(\tilde{K})$	χ^0	χ^0	χ^0
Neumann	χ^0	χ^0	χ^0	χ^0
Penalty on ϕ $\beta_\phi = \boldsymbol{\beta}_\phi h_K^{-3}$	$\boldsymbol{\beta}_\phi\chi^0$	* $\boldsymbol{\beta}_\phi\chi^0$	* $\boldsymbol{\beta}_\phi\chi^0$	* $\boldsymbol{\beta}_\phi\chi^0$
Nitsche on ϕ $\beta_\phi = \boldsymbol{\beta}_\phi(\chi h_K)^{-3}$	$\boldsymbol{\beta}_\phi\chi^{d-4}$	$\boldsymbol{\beta}_\phi\chi^{d-4}$	$\boldsymbol{\beta}_\phi\chi^{d-4}$	$\boldsymbol{\beta}_\phi\chi^{d-4}$
Penalty on $\nabla\phi\cdot\boldsymbol{n}$ $\beta_g = \boldsymbol{\beta}_g h_K^{-1}$	$\boldsymbol{\beta}_g\chi^0$	* $\boldsymbol{\beta}_g\chi^0$	* $\boldsymbol{\beta}_g\chi^0$	* $\boldsymbol{\beta}_g\chi^0$
Nitsche on $\nabla\phi\cdot\boldsymbol{n}$ $\beta_g = \boldsymbol{\beta}_g(\chi h_K)^{-1}$	$\boldsymbol{\beta}_g\chi^{d-2}$	** $\boldsymbol{\beta}_g\chi^{d-2}$	** $\boldsymbol{\beta}_g\chi^{d-2}$	** $\boldsymbol{\beta}_g\chi^{d-2}$
Nitsche on ϕ, $\beta_\phi = \boldsymbol{\beta} h_K^{-3}$ on $\nabla\phi\cdot\boldsymbol{n}$, $\beta_g = \boldsymbol{\beta}(\chi h_K)^{-1}$ and ghost $\gamma_K = \bar{\gamma}_K h^{2p-1}$	$\boldsymbol{\beta}\chi^0$	*** $\boldsymbol{\beta}\chi^0$	*** $\boldsymbol{\beta}\chi^0$	*** $\boldsymbol{\beta}\chi^0$

*: Adverse scaling with $\bar{\beta}$.
**: Unstable for $d = 1$.
***: Adverse scaling with $\bar{\beta}$, but only small $\bar{\beta}$ is required for sufficient accuracy.

The only difference compared to the results of the second-order problem, is that, in the case of mass lumping without mass scaling, this fourth-order problem requires at least quartic basis functions. For the analogous formulation for the second-order problem, quadratic basis functions were sufficient. This appears to hint at the more general condition $p \geq s$ (or, following Remark 3, $k + 1 \geq s$), with s the order of the spatial partial differential operator.

5. Numerical experiments

In this section, we present the results of our numerical experiments, which are designed to accomplish two objectives. First, in Section 5.1, we verify the derived scaling relations and conclusions from Sections 3 and 4.

Table 8
Resulting scaling with cut size for the first sliver-cut function for the fourth-order problem.

		Consistent mass (consistentmass)	Lumped mass (Eq. (14))	Consistent/lumped mass and ghost mass (Eq. (28)) with $\gamma_M = \bar{\gamma}_M h^{2p+1}$
	$\mathcal{O}(\tilde{M})$ / $\mathcal{O}(\tilde{K})$	χ^{2p+1}	χ^{p+1}	$\bar{\gamma}_M \chi^0$
Neumann	χ^{2p-3}	χ^{-4}	χ^{p-4}	$\bar{\gamma}_M^{-1}\chi^{2p-3}$
Penalty on ϕ $\beta_\phi = \boldsymbol{\beta}_\phi h_K^{-3}$	χ^{2p-3}	χ^{-4}	χ^{p-4}	$\bar{\gamma}_M^{-1}\chi^{2p-3}$
Nitsche on ϕ $\beta_\phi = \boldsymbol{\beta}_\phi(\chi h_K)^{-3}$	$\boldsymbol{\beta}_\phi \chi^{2p-3}$	$\boldsymbol{\beta}_\phi \chi^{-4}$	$\boldsymbol{\beta}_\phi \chi^{p-4}$	$\boldsymbol{\beta}_\phi \bar{\gamma}_M^{-1}\chi^{2p-3}$
Penalty on $\nabla\phi\cdot\boldsymbol{n}$ $\beta_g = \boldsymbol{\beta}_g h_K^{-1}$	χ^{2p-3}	χ^{-4}	* χ^{p-4}, $\boldsymbol{\beta}_g \chi^{p-3}$	$\bar{\gamma}_M^{-1}\chi^{2p-3}$
Nitsche on $\nabla\phi\cdot\boldsymbol{n}$ $\beta_g = \boldsymbol{\beta}_g(\chi h_K)^{-1}$	$\boldsymbol{\beta}_g \chi^{2p-3}$	$\boldsymbol{\beta}_g \chi^{-4}$	$\boldsymbol{\beta}_g \chi^{p-4}$	$\boldsymbol{\beta}_g \bar{\gamma}_M^{-1}\chi^{2p-3}$
Nitsche on ϕ, $\beta_\phi = \boldsymbol{\beta}_\phi h_K^{-3}$ on $\nabla\phi\cdot\boldsymbol{n}$, $\beta_g = \boldsymbol{\beta}_g(\chi h_K)^{-1}$ and ghost $\gamma_K = \bar{\gamma}_K h^{2p-1}$	$\bar{\gamma}_K \chi^0$	$\bar{\gamma}_K \chi^{-2p-1}$	$\bar{\gamma}_K \chi^{-p-1}$	$\bar{\gamma}_K \bar{\gamma}_M^{-1}\chi^0$

*: Even though the $(p-4)$-scaling is more severe, the $(p-3)$-scaling may dominate for small χ and/or large $\bar{\beta}_g$.

Table 9
Resulting scaling with cut size for the second sliver-cut function for the fourth-order problem.

		Consistent mass (Eq. (13a))	Lumped mass (Eq. (14))	Consistent/lumped mass and ghost mass (Eq. (28)) with $\gamma_M = \bar{\gamma}_M h^{2p+1}$
	$\mathcal{O}(\tilde{M})$ / $\mathcal{O}(\tilde{K})$	χ^0	χ^0	χ^0
Neumann	χ^0	χ^0	χ^0	χ^0
Penalty on ϕ $\beta_\phi = \boldsymbol{\beta}_\phi h_K^{-3}$	$\boldsymbol{\beta}_\phi \chi^0$	* $\boldsymbol{\beta}_\phi \chi^0$	* $\boldsymbol{\beta}_\phi \chi^0$	* $\boldsymbol{\beta}_\phi \chi^0$
Nitsche on ϕ $\beta_\phi = \boldsymbol{\beta}_\phi(\chi h_K)^{-3}$	$\boldsymbol{\beta}_\phi \chi^{-3}$	$\boldsymbol{\beta}_\phi \chi^{-3}$	$\boldsymbol{\beta}_\phi \chi^{-3}$	$\boldsymbol{\beta}_\phi \chi^{-3}$
Penalty on $\nabla\phi\cdot\boldsymbol{n}$ $\beta_g = \boldsymbol{\beta}_g h_K^{-1}$	$\boldsymbol{\beta}_g \chi^0$	* $\boldsymbol{\beta}_g \chi^0$	* $\boldsymbol{\beta}_g \chi^0$	* $\boldsymbol{\beta}_g \chi^0$
Nitsche on $\nabla\phi\cdot\boldsymbol{n}$ $\beta_g = \boldsymbol{\beta}_g(\chi h_K)^{-1}$	$\boldsymbol{\beta}_g \chi^{-1}$	$\boldsymbol{\beta}_g \chi^{-1}$	$\boldsymbol{\beta}_g \chi^{-1}$	$\boldsymbol{\beta}_g \chi^{-1}$
Nitsche on ϕ, $\beta_\phi = \boldsymbol{\beta} h_K^{-3}$ on $\nabla\phi\cdot\boldsymbol{n}$, $\beta_g = \boldsymbol{\beta}(\chi h_K)^{-1}$ and ghost $\gamma_K = \bar{\gamma}_K h^{2p-1}$	$\boldsymbol{\beta}\chi^0$	** $\boldsymbol{\beta}\chi^0$	** $\boldsymbol{\beta}\chi^0$	** $\boldsymbol{\beta}\chi^0$

*: Adverse scaling with $\bar{\beta}$.
**: Adverse scaling with $\bar{\beta}$, but only small $\bar{\beta}$ is required for sufficient accuracy.

Secondly, we assess whether the presence of the ghost-stabilized mass negatively impacts the error behavior and convergence characteristics of the explicit scheme. To this end, we examine a linear vibrating drum in Section 5.2 and a linear Kirchhoff–Love shell in Section 5.3.

5.1. Verification of time-step size scaling

To numerically verify the scaling relations collected in Tables 1–4 and 6–9, we consider the two-dimensional domain illustrated in Fig. 7. The figure shows the mesh that is used for all subsequent computations, with the ghost faces highlighted. The domain cut-out involves straight edges, curved edges and positive and negative corner cuts,

Table 10
Overview of the stability characteristics for the fourth-order problem. Worst-case scaling of the cut scenarios considered in Tables 6, 8 and 9.

	Consistent mass (Eq. (13a))	Lumped mass (Eq. (14))	Consistent/lumped mass and ghost mass (Eq. (28)) with $\gamma_M = \bar{\gamma}_M h^{2p+1}$
Neumann		Unstable for $p \in \{2, 3\}$	
Penalty on ϕ $\beta_\phi = \boldsymbol{\beta}_\phi h_K^{-3}$		Unstable for $p \in \{2, 3\}$ Scales with $\boldsymbol{\beta}$	Scales with $\boldsymbol{\beta}_\phi$
Nitsche on ϕ $\beta_\phi = \boldsymbol{\beta}_\phi (\chi h_K)^{-3}$			
Penalty on $\nabla\phi \cdot \boldsymbol{n}$ $\beta_g = \boldsymbol{\beta}_g h_K^{-1}$		Unstable for $p \in \{2, 3\}$ Scales with $\boldsymbol{\beta}$	Scales with $\boldsymbol{\beta}_g$
Nitsche on $\nabla\phi \cdot \boldsymbol{n}$ $\beta_g = \boldsymbol{\beta}_g (\chi h_K)^{-1}$			
Nitsche on ϕ, $\beta_\phi = \boldsymbol{\beta} h_K^{-3}$ on $\nabla\phi \cdot \boldsymbol{n}$, $\beta = \boldsymbol{\beta}_g (\chi h_K)^{-1}$ and ghost $\gamma_K = \bar{\gamma}_K h^{2p-1}$			Requires $\bar{\gamma}_M \sim \bar{\gamma}_K$ and small $\boldsymbol{\beta}$

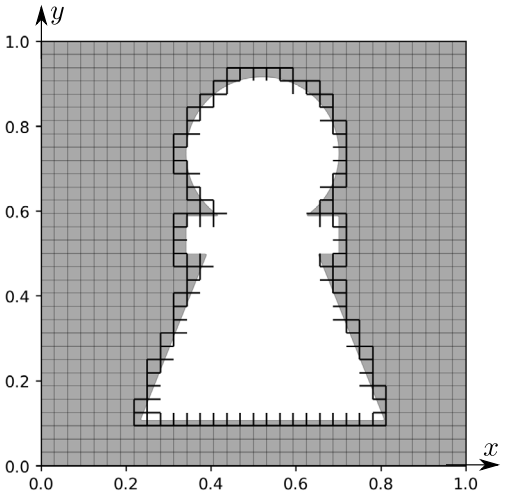

Fig. 7. Domain, cut-out, mesh and ghost faces.

such that a wide variety of cut configurations may occur. To generate different cases, we randomly displace the cut-out within the domain by a distance between $-h_K$ and h_K in the x and y directions. For each new domain, we compute the critical time-step, as defined in Eq. (1), for the different formulations and polynomial orders. All computations are performed with row-sum mass-lumped mass matrices (apart from the ghost-mass term, as addressed in Remark 2).

5.1.1. Neumann boundaries

Figs. 8 and 9 present the results for the case where the entire cut-boundary is a Neumann boundary, for the second- and fourth-order equation, respectively. Figs. 8(a) and 9(a) involve basis functions with the lowest permitted polynomial order ($p = 1$, respectively $p = 2$), and in Figs. 8(b) and 9(b) this order is incremented by one. The blue dashed lines in these figures correspond to the case without a cut-out, representing the optimal achievable value. We note that these 'optimal' values do still suffer from the usual boundary outliers due to the repeating knots at the exterior boundary [21,54,60], but believe that this represents the relevant comparison. The black dotted lines indicate the anticipated scaling relations derived in the preceding analysis sections.

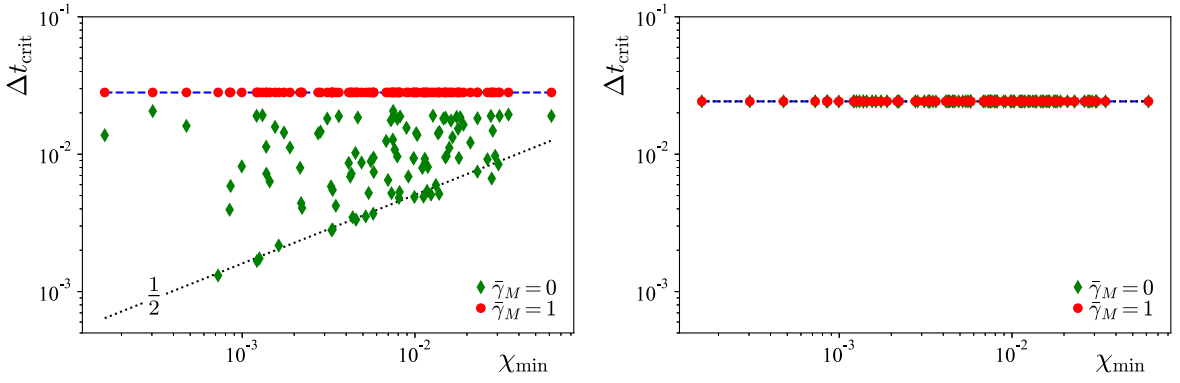

(a) $p = 1$. **(b)** $p = 2$.

Fig. 8. Neumann formulation of the second-order equation: first row in Tables 1–5. Critical time-step size dependency on the minimal element size fraction for 100 perturbations of the domain of Fig. 7.

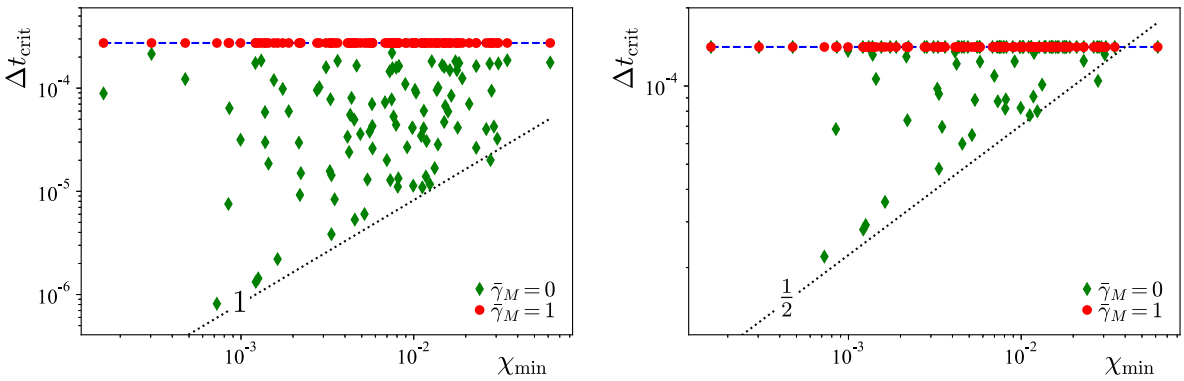

(a) $p = 2$. **(b)** $p = 3$.

Fig. 9. Neumann formulation of the fourth-order equation: first row in Tables 6–10. Critical time-step size dependency on the minimal element size fraction for 100 perturbations of the domain of Fig. 7.

For a row-sum lumped mass matrix without ghost-stabilized mass, the scaling of the maximum eigenvalue is predicted to be χ^{p-s}, according to Tables 3 and 8, where $s \in \{2, 4\}$ is the order of the spatial differential operator. The critical time-step size relates to the maximum eigenvalue according to $\Delta t_{\text{crit}} \propto (\lambda^h_{\max})^{-\frac{1}{2}}$, and should thus scale as $\chi^{\frac{1}{2}(s-p)}$. As the black dotted lines indicate, this is indeed the trend that the bottom green diamonds follow. Not all data points follow this trend, since the smallest χ in the domain (on the horizontal axis) may correspond to a corner-cut function instead, which, according to Tables 1 and 6, does not cause adverse scaling.

According to the results presented in Tables 5 and 10, the cut-size dependency of the critical time-step size can be mitigated by raising the polynomial to $p \geq s$, or by incorporation the ghost-mass term. The latter approach is confirmed to be effective in all plots, as indicated by the red markers, and the former approach is demonstrated in Fig. 8(b). For unfavorably cut elements, both methods have the potential to increase the critical time-step size by orders of magnitude. For the second-order equation, quadratic basis functions are sufficient to achieve this effect, but quartic basis functions are required to eliminate the scaling for the fourth-order (shell-type) equation. In the event that the use of such high-order basis functions is not feasible, the ghost-mass term serves as an alternative solution.

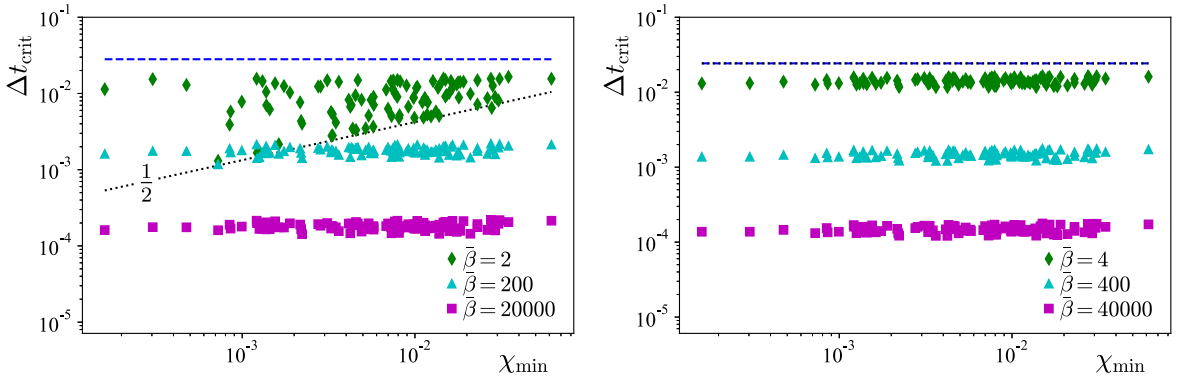

(a) $p = 1$. **(b)** $p = 2$.

Fig. 10. Penalty formulations without ghost-stabilized mass for the second-order problem: second row and second column in Tables 1–5. Critical time-step size dependency on the minimal element size fraction for 100 perturbations of the domain of Fig. 7.

5.1.2. Penalty formulations

If the cut-boundary is a Dirichlet boundary instead, and a penalty method is used for the enforcement of the constraints, then, according to Tables 4 and 9, the maximum eigenvalue scales with $\bar{\beta}$. This is confirmed in Figs. 10 and 11 for basis functions with different polynomial orders for the second- and fourth-order problems, respectively. For $p \leq s$ ($s \in \{2, 4\}$ the order of the spatial differential operator) the first sliver-cut function (Tables 3 and 8) also introduces a scaling of the critical time-step with $\chi^{\frac{1}{2}(s-p)}$ in the same manner as for the Neumann boundary formulation. Both types of scaling are observed in the various subfigures: for $p < s$ and small $\bar{\beta}$ the markers follow the black dotted line, but as $\bar{\beta}$ is increased the second sliver-cut functions produce the highest eigenvalues and the dependency on χ is no-longer dominant in the considered collection of cut cases.

We notice that the data-points in Fig. 11(c) are more scattered than those in the other figures, which can be attributed to the two types of scaling of the first sliver-cut function identified in Table 8. Additional dash-dotted lines are added to highlight the second, $(\bar{\beta}_g^{-\frac{1}{2}}\chi^{\frac{1}{2}(3-p)})$-order, scaling.

Addition of the ghost-mass term only suppresses the $\chi^{\frac{1}{2}(s-p)}$-scaling, as it did for the pure Neumann formulation. This means that significant critical time-step size improvements can be achieved for small $\bar{\beta}$ values, or when $p < s$ (from Figs. 10(a) to 12(a), from Figs. 11(a) and 11(c) to Fig. 13(a), and from Figs. 11(b) and 11(d) to Fig. 13(b)), but not for larger penalty values, or when $p \geq s$.

5.1.3. Nitsche formulations

The results of the various Nitsche formulations are presented in Figs. 14 and 15 for the second- and fourth-order problem, respectively. Figs. 14(a), 15(a) and 15(c) correspond to Nitsche formulations with penalty parameters that are chosen per the inverse estimates of Eqs. (21), (40a) and (40b), which thus involve the local element size measure $h_c = \chi\, h_K$. The four functions on cut elements induce different scaling orders. According to Tables 1 and 6, the first corner-cut function causes a $(\chi^{\frac{1}{2}(s-pd)})$-order scaling. For the considered combinations of s, p and d, this reduces to a scaling with χ^0 for all cases. This zeroth-order scaling is observed in Figs. 14(a) and 15(c), but not in Fig. 15(a). For the Nitsche formulation used in Fig. 15(a), the scaling induced by the *second* corner-cut function dominates, as found in Table 7. Furthermore, the first sliver-cut function induces a scaling of order $\chi^{\frac{1}{2}(s-p)}$ according to Tables 3 and 8, and the second sliver-cut function induces a scaling of order $\chi^{\frac{1}{2}}$ (Figs. 14(a) and 15(c)) or $\chi^{\frac{3}{2}}$ (Fig. 15(a)) according to Tables 4 and 9. These latter scalings are independent of p, and therefore increasing the polynomial order will not improve the results. All predicted scaling trends are plotted in each of the three subfigures (sometimes overlapping) confirming that they are indeed bounds of the obtained critical time-step size.

In Figs. 14(b), 15(b) and 15(d), the results are plotted for the Nitsche formulations with penalty parameter that scale with the inverse of h_K. These formulations incorporate a ghost-penalty term in the stiffness matrix to guarantee a its positive definiteness. According to Tables 1 and 6, a function on a corner-cut element induces a detrimental

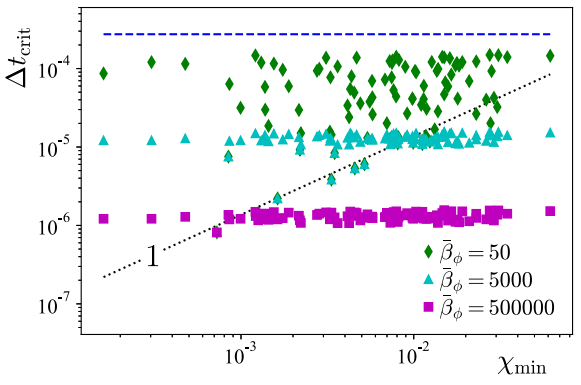

(a) On ϕ, $p = 2$.

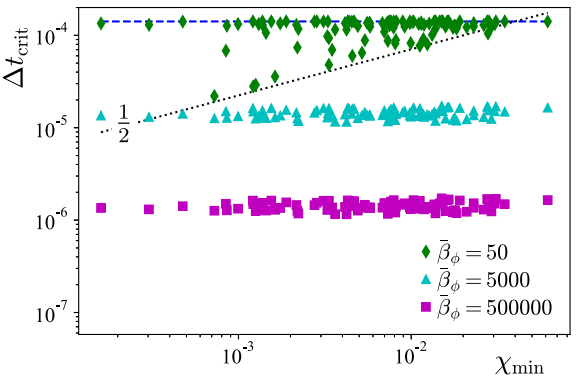

(b) On ϕ, $p = 3$.

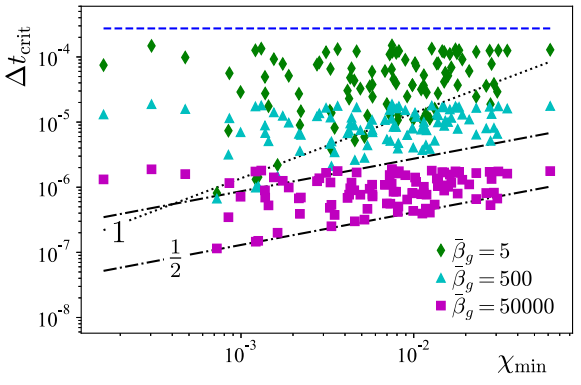

(c) On $\nabla\phi \cdot \boldsymbol{n}$, $p = 2$.

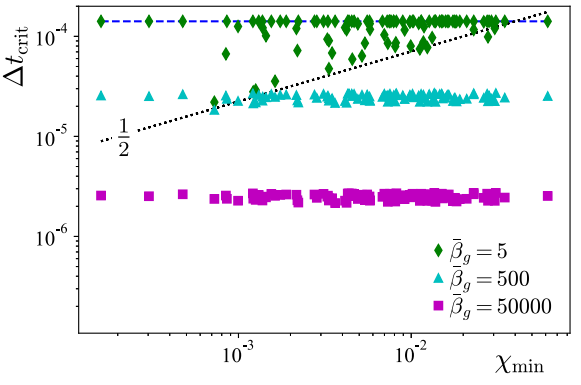

(d) On $\nabla\phi \cdot \boldsymbol{n}$, $p = 3$.

Fig. 11. Penalty formulations without ghost-stabilized mass for the fourth-order problem: second and fourth row and second column in Tables 6–10. Critical time-step size dependency on the minimal element size fraction for 100 perturbations of the domain of Fig. 7.

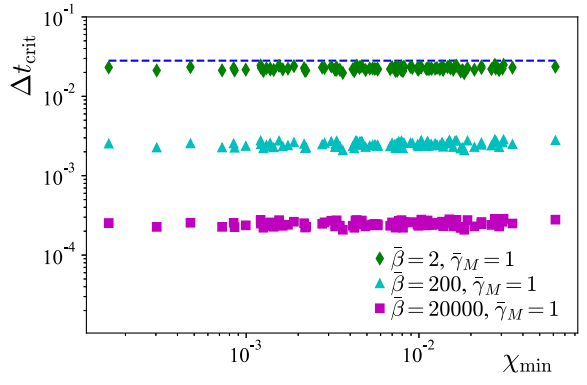

(a) $p = 1$.

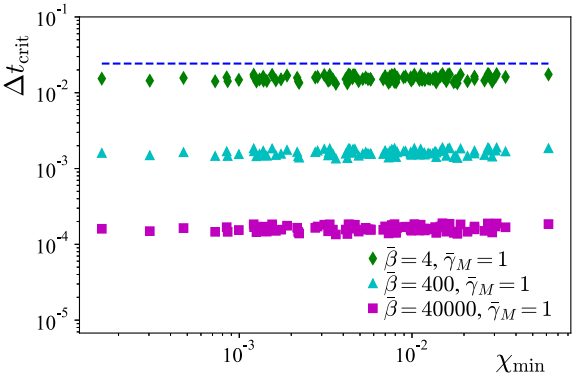

(b) $p = 2$.

Fig. 12. Penalty formulations with ghost-stabilized mass for the second-order problem: second row and third column in Tables 1–5. Critical time-step size dependency on the minimal element size fraction for 100 perturbations of the domain of Fig. 7.

cut-size dependency of the critical time-step size of order $\chi^{\frac{1}{2}(pd+d)}$. Similarly, the first sliver-cut function causes a scaling of the order $\chi^{\frac{1}{2}(p+1)}$ as stated in Tables 3 and 8. Both these trends are plotted in each of the respective

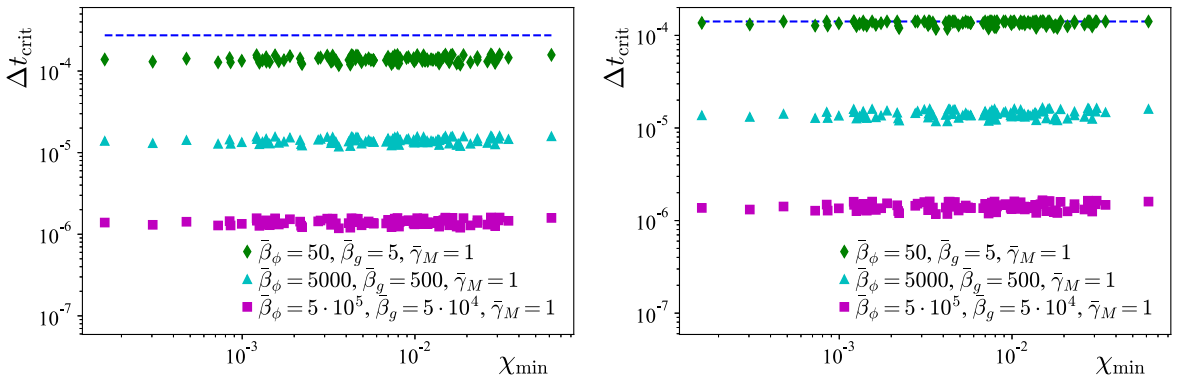

(a) $p = 2$. **(b)** $p = 3$.

Fig. 13. Penalty formulations for both ϕ and $\nabla\phi \cdot \boldsymbol{n}$ with ghost-stabilized mass for the fourth-order problem: second and fourth row and third column in Tables 6–10. Critical time-step size dependency on the minimal element size fraction for 100 perturbations of the domain of Fig. 7.

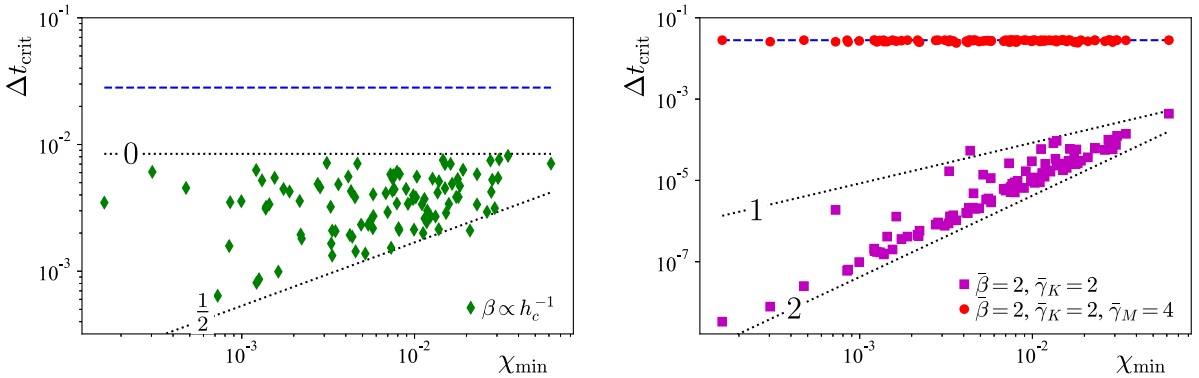

(a) With β according to Eq. (21). **(b)** With ghost penalty stabilization.

Fig. 14. Nitsche formulations for the second-order problem, for $p = 1$: third and fourth row and second and third column in Tables 1–5. Critical time-step size dependency on the minimal element size fraction for 100 perturbations of the domain of Fig. 7.

subfigures. The positive exponent p in these relations implies that this scaling will only worsen with increasing polynomial order. However, the addition of the ghost-mass term eliminates the cut-size dependency altogether. The highest eigenvalue does still scale with $\bar{\beta}\chi^0$. In Fig. 15(b) we observe that the red markers exhibit a smaller critical time-step size than the maximally achievable value indicated by the dashed-blue line. This indicates that the penalty value required to stabilized the Nitsche formulation is not sufficiently small to avoid affecting the highest eigenvalues.

5.2. *Convergence of a linear pre-stressed membrane*

The results of the analysis on the scaling of the critical time-step size with the cut-element size indicate that addition of ghost-stabilized mass can, in certain cases, significantly increase the critical time-step size. In particular, it enables a Nitsche formulation with a cut-size independent critical time-step size. Of course, the added ghost-stabilized mass should not come at the cost of a severe accuracy reduction. In this section, we study the impact of the added ghost-stabilized mass on the solution error for a linear pre-stressed membrane, i.e., for the second-order wave equation of Section 3. We consider the same geometry description as before, depicted in Fig. 7, and take as

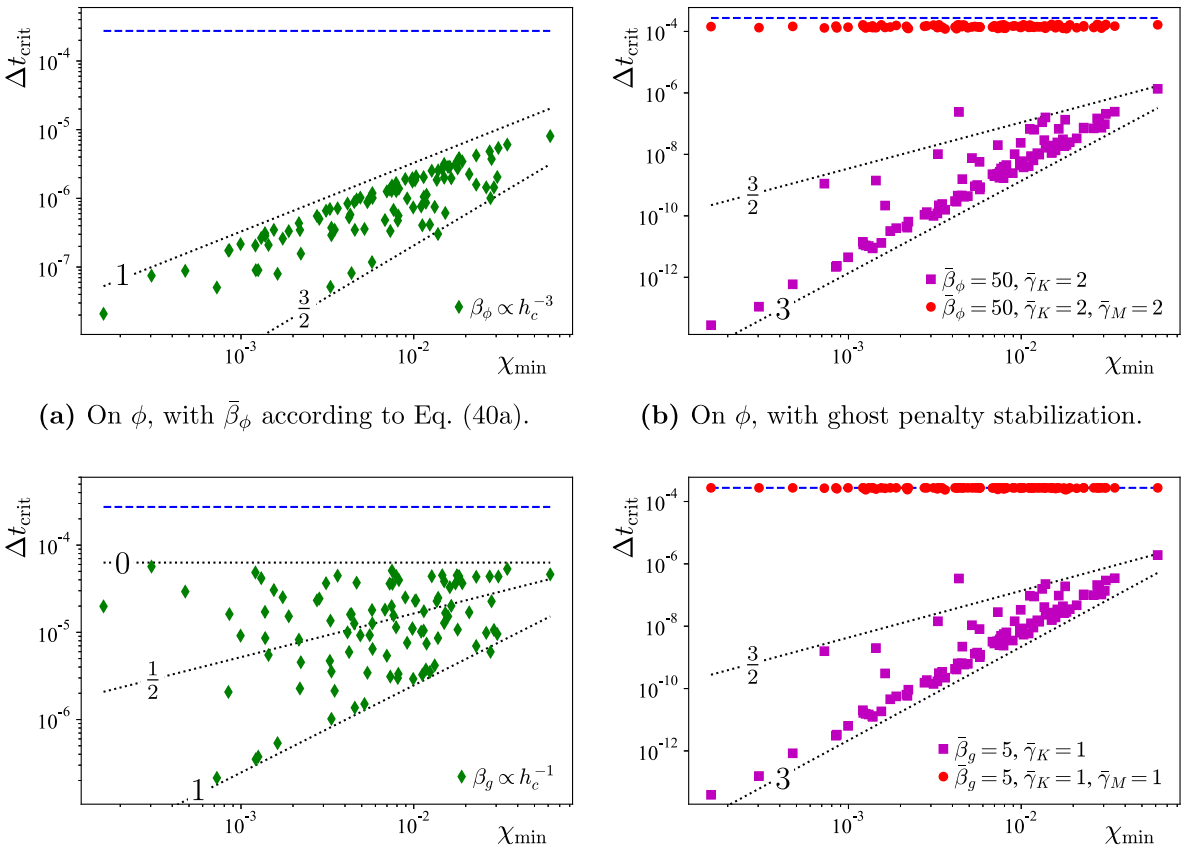

(a) On ϕ, with $\bar{\beta}_\phi$ according to Eq. (40a).

(b) On ϕ, with ghost penalty stabilization.

(c) On $\nabla\phi \cdot \boldsymbol{n}$, with $\bar{\beta}_g$ according to Eq. (40b).

(d) On $\nabla\phi \cdot \boldsymbol{n}$, with ghost penalty stabilization.

Fig. 15. Nitsche formulations for the fourth-order problem, for $p = 2$: third, fourth and fifth row and second and third column in Tables 6–10. Critical time-step size dependency on the minimal element size fraction for 100 perturbations of the domain of Fig. 7.

an exact solution a simple standing sine wave:

$$\phi_{\text{exact}}(t, x, y) = \cos(\sqrt{2}\pi t)\sin(\pi x)\sin(\pi y)\,, \tag{42}$$

from which we infer the required initial and boundary conditions. In the following, we compute one full period of this oscillation, for which we use a Newmark-type central difference method for time integration. This limits the optimal convergence rates to second-order, which, due to mass lumping, is the highest order of convergence regardless [56,60].

First, we investigate the scenario where the entire cut-out represents a Neumann boundary. According to Table 5, and as verified in Fig. 8(a), the addition of ghost-stabilized mass only affects the critical time-step size for the $p = 1$ order of basis functions. Fig. 16 shows the convergence curves of the relative H_0^1 and L^2-errors for the formulations with and without a ghost-mass term. The dashed-blue lines indicate the optimal orders of convergence. The numbers attached to the final markers in the L^2-error graphs denote the total number of time steps required to carry out the corresponding simulation. For this particular example, we observe a factor 3 reduction of the required number of time steps on the most refined grid. Despite this reduction, we observe that the addition of the ghost-mass term does not compromise the accuracy of the approximation.

Next, we consider penalty methods with different penalty factors, without ghost-stabilized mass. The error convergence curves for $p = 1$ and $p = 2$ are shown in Fig. 17. For both polynomial orders, the smallest chosen penalty parameter only marginally impacts the critical time-step size, as may be ascertained from Fig. 10. As a result, the $p = 1$ simulation on the most refined grid requires $\sim 5\%$ more time steps than the corresponding Neumann case plotted in Fig. 16. At the same time, the error has increased significantly. This is in part due to the variational

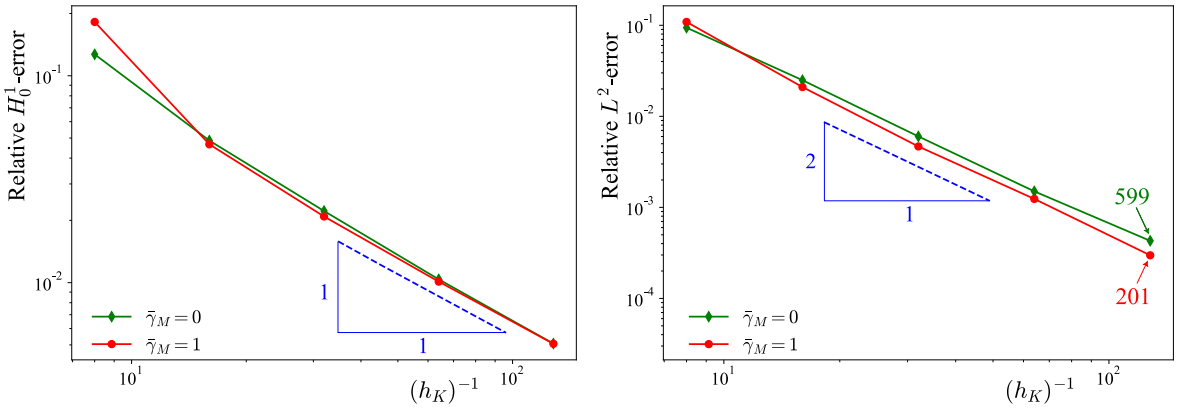

(a) H_0^1-error. **(b)** $L2$-error.

Fig. 16. Error convergence for a vibrating pre-stressed membrane on the domain of Fig. 7 after one full period of oscillation, for the Neumann case with and without ghost-stabilized mass, with $p = 1$.

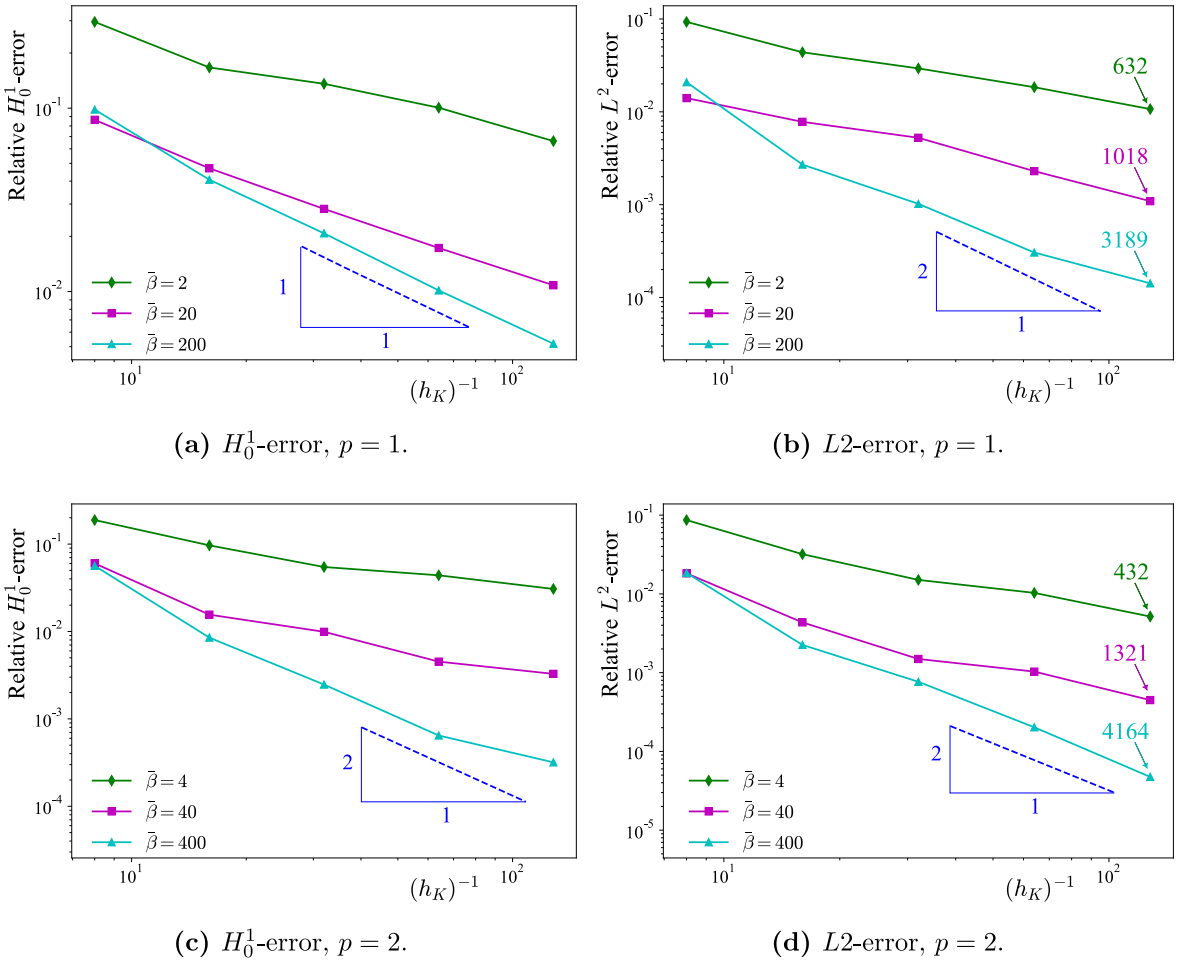

(a) H_0^1-error, $p = 1$. **(b)** $L2$-error, $p = 1$.

(c) H_0^1-error, $p = 2$. **(d)** $L2$-error, $p = 2$.

Fig. 17. Error convergence for a vibrating pre-stressed membrane on the domain of Fig. 7 after one full period of oscillation, for penalty methods with different penalty factors.

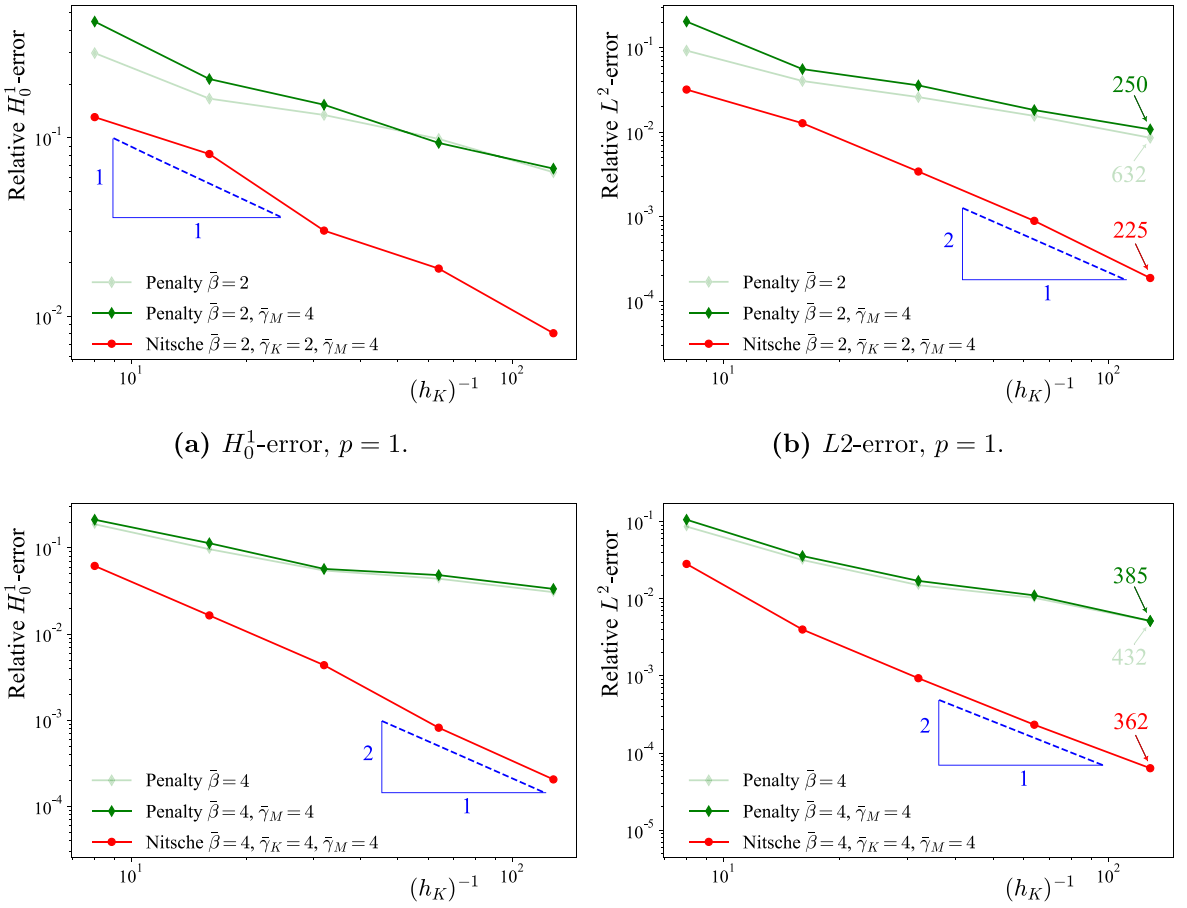

(a) H_0^1-error, $p=1$. **(b)** $L2$-error, $p=1$.

(c) H_0^1-error, $p=2$. **(d)** $L2$-error, $p=2$.

Fig. 18. Error convergence for a vibrating pre-stressed membrane on the domain of Fig. 7 after one full period of oscillation, for Nitsche or penalty enforcement of Dirichlet constraints.

inconsistency of the penalty formulation, which causes a loss of the optimal (spatial) convergence rate. The errors may be reduced by several orders of magnitude by increasing the penalty parameter. However, an increase of the penalty parameter comes at the cost of a reduced critical time-step size. In particular, we observe a factor 5 (for $p=1$) and 10 (for $p=2$) increase of the required total number of time steps for a factor 100 increase in $\bar{\beta}$. At the highest penalty level, the optimal orders of convergence appear to be achieved in some of the subfigures, but these convergence rates drop past a certain mesh refinement level. In Fig. 17(d), the optimal, third-order, convergence rate is not attained due to the use of the second-order central-difference time stepping scheme and the use of mass lumping.

Finally, we compare the performance of a penalty method with that of a Nitsche formulation. To ensure an equitable comparison, both formulations are augmented with ghost-stabilized mass and make use of the same penalty parameter values. As a result, the simulation with Nitsche's method and the simulation with the penalty method require a comparable number of times steps. The relative H_0^1 and L^2-errors are plotted in Fig. 18, for $p=1$ and $p=2$. For reference, the results of the penalty methods without ghost-stabilized mass from Fig. 17 are overlaid. As anticipated, the addition of the ghost-stabilized mass to the penalty method for these moderate penalty parameter values reduces the required number of time steps significantly for $p=1$ and only little for $p=2$. In both cases, the ghost-stabilized mass only marginally affects accuracy. A jump in solution quality is achieved by switching to the Nitsche formulation. Due to the variational consistency of the formulation, both the H_0^1 and L^2-errors converge optimally, yielding error reductions by orders of magnitude on the finer meshes. The exception is again Fig. 17(d),

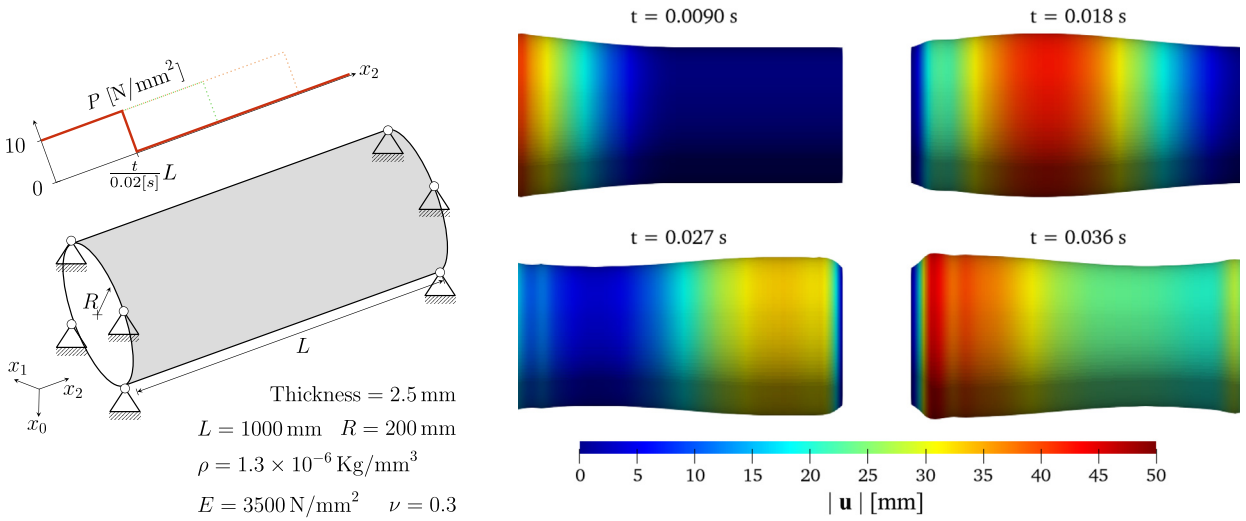

(a) Problem description. (b) Transient solution.

Fig. 19. Kirchhoff–Love shell model problem.

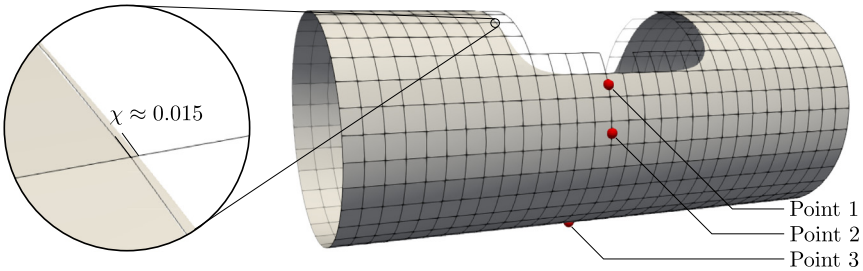

Fig. 20. Immersed domain and mesh of 30 × 30 elements, with filleted rectangular cut-out. Indicated points are measurement locations referenced in Fig. 23.

for which the rate of convergence is limited to two, owing to the second-order time-stepping scheme and the mass lumping. For $p = 1$, the error values even closely resemble those of the pure Neumann case in Fig. 16.

5.3. Transient response of a linear Kirchhoff–Love shell

To demonstrate the practical applications of ghost-stabilized mass and Nitsche's method, we examine their usage in a transient simulation of a Kirchhoff–Love shell [7,61]. As a case study, we consider a pressure shock-wave propagating through a pipe-segment with pinned support on both ends. Fig. 19(a) shows the geometry, the material parameters and the load-function. The shock-wave travels through the entire pipe-segment in 0.02 s. Fig. 19(b) shows the resulting displacement field of a reference computation, computed on a 30 × 30 grid of $p = 2$ polynomial B-splines.

We then create a rectangular cut-out with corner fillets at the center of the cylinder, as depicted in Fig. 20, and treat the corresponding interior edges as immersed boundaries (or, trimmed patches). To repeat the simulation of the traveling shock-wave, we use the reference solution depicted in Fig. 19(b) as the manufactured solution for prescribing boundary conditions at these internal edges. Specifically, we extract the in-plane and out-of-plane displacement vectors and the normal rotation of the shell at the integration points around the cut-out. These three fields represent essential boundary conditions for the Kirchhoff–Love shell model. In the immersogeometric computations, we enforce all conditions with either a penalty method or with Nitsche's method. The exact Nitsche formulation that we adopt can be found in [62].

Table 11
Critical time-step sizes for the different Kirchhoff–Love shell simulations.

Method	Uncut	Penalty formulation	Penalty formulation, with ghost mass	Nitsche formulation, with ghost mass
Δt_{crit} [ms]	0.475	0.0311	0.393	0.475

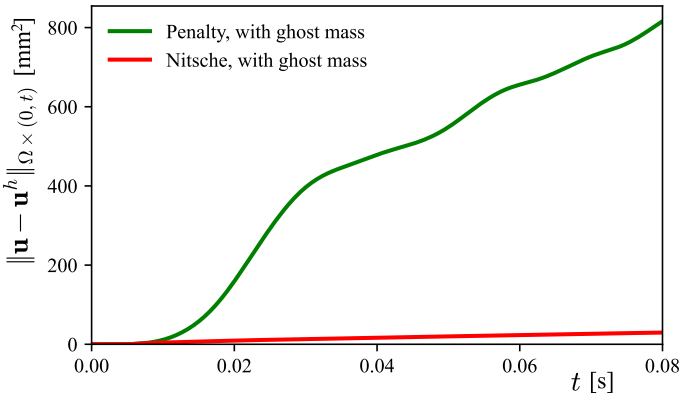

Fig. 21. Evolution of the error in the Bochner norm for the penalty and Nitsche formulations of the Kirchhoff–Love shell.

For both a penalty formulation and a Nitsche formulation, the three essential conditions all require a respective penalty parameter; β_1 for the out-of-plane displacement, β_2 for the normal rotation, and β_3 for the in-plane displacement. In [62], β_1 is referred to as $C^S_{\text{pen},1}$, β_2 as $C^S_{\text{pen},3}$, and β_3 as $C^S_{\text{pen},4}$. In the subsequent numerical experiments, we choose these penalty parameters as $\beta_1 = 50$, $\beta_2 = 15$, and $\beta_3 = 2.5$ for both the penalty formulations and the Nitsche formulation. The ghost penalty parameters for the contributions to the stiffness matrix (for the in-plane displacement as well as for the out-of-plane displacement field) and to the mass matrix are all set to 0.1. These penalty values are obtained through the following procedure. First, the γ_K and β penalty parameters are chosen excessively high, and the γ_M parameter is set to zero. Then, we reduce the β-penalty parameters until they reach a threshold past which the smallest system eigenvalue becomes negative. After fixing the β penalty parameters at their respective values just above these threshold levels, we reduce the ghost-stiffness parameters to their lowest value for which positivity of the smallest eigenvalue is still retained. Finally, we increment γ_M until an increase thereof no longer affects the maximum system eigenvalue.

Table 11 presents the critical time-step sizes for the various formulations for the example of Fig. 20, which concerns a background mesh consisting of 30×30 quadratic B-spline elements. As the critical time-step sizes in the table show, the use of ghost-stabilized mass for the penalty method increases the critical time-step size by more than 15 times. With the Nitsche formulation, we retrieve a critical time-step size equal to that of the uncut case, which is the optimal value.

The traveling shock-wave computations are executed at the respective critical time-step size of each formulation. The evolution of the error over time is captured by the following time-dependent Bochner norm:

$$\|\boldsymbol{u} - \boldsymbol{u}^h\|_{\Omega\times(0,t)} = \frac{1}{t}\int_0^t \|\boldsymbol{u}(\tau,\cdot) - \boldsymbol{u}^h(\tau,\cdot)\|_{L^2(\Omega)}\,\mathrm{d}\tau\,. \tag{43}$$

The progression of this error is plotted in Fig. 21 for both the penalty formulation and the Nitsche formulation. The adoption of the Nitsche formulation results in a reduction of the error by well over an order of magnitude. The manifestation of the error is depicted in Fig. 22 for time $t = 0.045$. The deviation from the expected physical response is significantly more pronounced for the penalty formulation than for the Nitsche formulation (also note the change in the range of the colorbar in this regard). In particular, the error distribution in Fig. 22(a) indicates that penalty enforcement of the boundary conditions not only locally impacts the solution, but in fact disturbs the complete solution field. In contrast, the far-field impact of the Nitsche-based weak boundary condition enforcement is almost negligible, owing to its variational consistency.

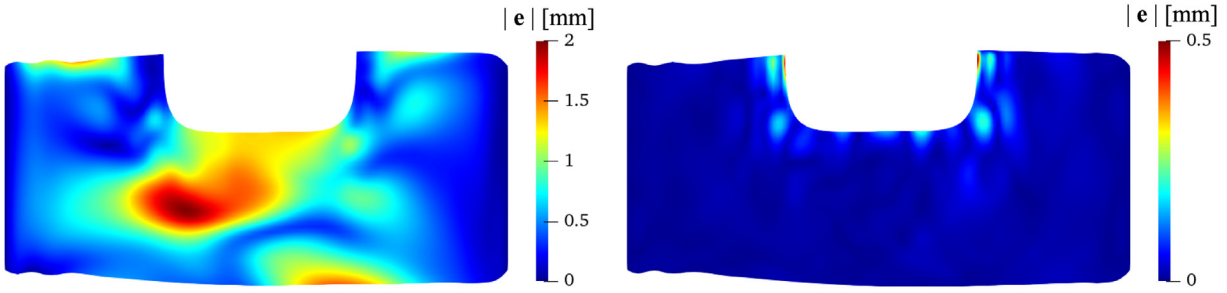

(a) Penalty formulation, with ghost-stabilized mass. (b) Nitsche formulation, with ghost-stabilized mass.

Fig. 22. Magnitude of the displacement error in mm, at $t = 0.045$s.

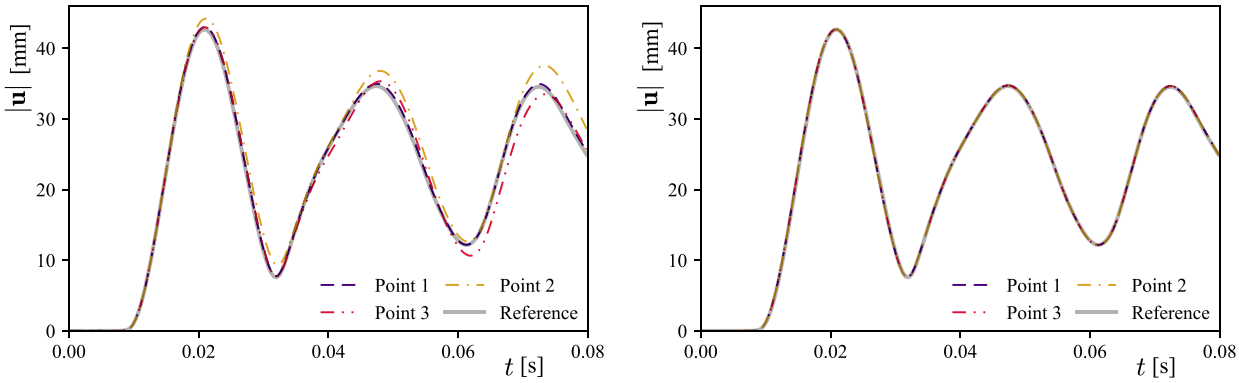

(a) Penalty formulation, with ghost-stabilized mass. (b) Nitsche formulation, with ghost-stabilized mass.

Fig. 23. Displacement magnitude over time at the three point locations indicated in Fig. 20.

It can also be inferred from the error distribution that the axisymmetric nature of the true solution, as depicted in Fig. 19(b), is lost in both finite element approximations. This loss is quantitatively assessed in Fig. 23, which plots the displacement magnitudes at the three locations along the span of the cylinder indicated in Fig. 20. The results for the penalty method are shown in Fig. 23(a), while those for the Nitsche formulation are shown in Fig. 23(a). For the penalty method, the displacement magnitudes at the three points deviate increasingly from the reference solution, and also diverge with respect to each other. This erroneous behavior is significantly suppressed when the Nitsche formulation is adopted, as evidenced by the nearly overlapping displacement curves for all points.

6. Conclusion and outlook

Immersogeometric explicit analysis offers a powerful framework for streamlining the design-to-analysis pipeline for crash-test type simulations. To ensure a robust and reliable pipeline, it is imperative that the critical time-step size of the explicit time-stepping scheme is not affected by the size of the cut (or "trimmed") elements. In this article, we have studied the dependency of the critical time-step size on the cut-size for different types of boundary conditions and different methods of enforcement. The formulations that we investigated include a pure Neumann problem, penalty enforcement of Dirichlet constraints, and Nitsche's method for enforcement of Dirichlet constraints. To ensure a positive definite stiffness matrix when Nitsche's method is used, we considered a formulation where the Nitsche penalty parameter is determined based on an element-local eigenvalue problem, leading to a cut-size dependent penalty parameter, and a formulation with an additional ghost-penalty term, which then permits a cut-size independent penalty parameter. For each formulation, we considered a consistent mass matrix and a row-sum lumped mass matrix, both with and without additional ghost-penalty based mass scaling ("ghost-stabilized mass").

We have found that a formulation with a consistent mass matrix, without any form of mass scaling, always suffers from adverse scaling of the critical time-step size with element cut-size. As was first observed in [21], this

problematic scaling is mitigated by row-sum mass lumping, but only when the polynomial order of the maximum regularity splines is sufficiently high. Our analysis confirms this observation: for a second-order and a fourth-order equation we show that mass lumping alone is insufficient when the order of the basis functions is lower than the order of the spatial differential operator. To enable 'lower-order' discretization (i.e., up to cubics for shell-type equations), an additional mass scaling is required. The cut-size dependency vanishes for our proposed addition of ghost-stabilized mass.

Our analysis also shows that penalty enforcement of Dirichlet conditions suffers from the drawback that the critical time-step size scales with the penalty parameter after a threshold value, confirming the observations in [5,21]. Despite this drawback, a penalty formulation combined with mass-lumping and spline basis functions of sufficiently high regularity is the only formulation for enforcement of Dirichlet conditions that does not require an additional form of mass scaling to mitigate the dependence on the cut-element size. While the critical time-step size also scales linearly with the penalty parameter for Nitsche's method for enforcement of Dirichlet conditions, the penalty factors required to achieve satisfactory results are generally significantly lower. Out of the different Nitsche formulations that we considered, the only formulation for which the critical time-step size is independent of the cut-element size is one with ghost-stabilized stiffness and ghost-stabilized mass. For a linear wave equation and a linear Kirchhoff–Love shell model, we have shown that the enforcement of Dirichlet conditions with this Nitsche formulation, as opposed to a penalty method, may lead to reductions of the solution error by orders of magnitude at the same (or higher) critical time-step size.

A favorable property of ghost-stabilized mass at the problematically cut elements in comparison to more conventional mass-scaling methods, is that it does not suffer from severe variational inconsistency issues. With numerical experiments, we have demonstrated that ghost-stabilized mass can be utilized without incurring negative impact on solution quality, despite a potentially substantial increase in the critical time-step size, sometimes by orders of magnitude. The glaring defect of ghost-stabilized mass in its current form is that it impairs the diagonality of the lumped mass matrix at cut boundaries. Such a diagonal structure is imperative for developing fast solvers, as it guarantees a sparse inverse matrix that is trivial to compute. As the ghost-stabilized mass only acts on the elements intersecting the boundary, which is generally a small fraction of the elements, it only locally affects the sparsity-level of the inverse matrix. Nevertheless, an open research question pertains to the efficient (approximate) inversion of the mass matrix when ghost-stabilized mass is added to the formulation. A promising approach could be to add the ghost-stabilized mass patchwise, with the aim of producing a block diagonal mass matrix with small blocks, facilitating explicit inversion with blockwise LU decomposition. Further suggestions have been made in Remark 2.

Declaration of competing interest

The authors declare that they have no known competing financial interests or personal relationships that could have appeared to influence the work reported in this paper.

Data availability

Data will be made available on request.

Acknowledgments

S.K.F. Stoter gratefully acknowledges financial support through the Industrial Partnership Program Fundamental Fluid Dynamics Challenges in Inkjet Printing (FIP), a joint research program of Canon Production Printing, Eindhoven University of Technology, University of Twente, and the Netherlands Organization for Scientific Research (NWO). C.V. Verhoosel and S.C. Divi acknowledge the partial support of the European Union's Horizon 2020 research and innovation programme under Grant Agreement No 101017578 (SIMCor). M. Larson and E.H. van Brummelen gratefully acknowledge the insightful discussions at the special session organized by Prof. Trond Kvamsdal at IGA 2022 in Banff. All simulations have been performed using the open source software package Nutils [63].

References

[1] J.O. Hallquist, LS-DYNA theory manual No. March, Livermore Software Technology Corporation, 2006.

[2] M. Smith, ABAQUS/Standard User's Manual, Version 6.6, Dassault Systèmes Simulia Corp, United States, 2009.

[3] Ansys Explicit Dynamics, URL www.ansys.com/content/dam/product/structures/ansys-explicit-dynamics-brochure-140.pdf.

[4] J.A. Cottrell, T.J.R. Hughes, Y. Bazilevs, Isogeometric Analysis: Toward Integration of CAD and FEA, first ed., John Wiley & Sons, 2009.

[5] L.F. Leidinger, M. Breitenberger, A.M. Bauer, S. Hartmann, R. Wüchner, K.U. Bletzinger, F. Duddeck, L. Song, Explicit dynamic isogeometric B-Rep analysis of penalty-coupled trimmed NURBS shells, Comput. Methods Appl. Mech. Engrg. 351 (2019) http://dx.doi.org/10.1016/j.cma.2019.04.016.

[6] LS-DYNA: Keyword User Manual, LS-DYNA R8.0 Keyword User's Manual - Volume III - Multi-Physics Solvers, vol. I, Livermore Software Technology Corporation, 2021.

[7] J. Kiendl, K.U. Bletzinger, J. Linhard, R. Wüchner, Isogeometric shell analysis with Kirchhoff-Love elements, Comput. Methods Appl. Mech. Engrg. 198 (49–52) (2009) http://dx.doi.org/10.1016/j.cma.2009.08.013.

[8] J. Kiendl, F. Auricchio, T.J.R. Hughes, A. Reali, Single-variable formulations and isogeometric discretizations for shear deformable beams, Comput. Methods Appl. Mech. Engrg. 284 (2015) 988–1004.

[9] T.J.R. Hughes, J.A. Evans, A. Reali, Finite element and NURBS approximations of eigenvalue, boundary-value, and initial-value problems, Comput. Methods Appl. Mech. Engrg. 272 (2014) http://dx.doi.org/10.1016/j.cma.2013.11.012.

[10] V. Puzyrev, Q. Deng, V. Calo, Spectral approximation properties of isogeometric analysis with variable continuity, Comput. Methods Appl. Mech. Engrg. 334 (2018) http://dx.doi.org/10.1016/j.cma.2018.01.042.

[11] L. Brillouin, Wave Propagation in Periodic Structures, first ed., in: International Series in Pure and Applied Physics, Dover Books, 1946.

[12] A. Hansbo, P. Hansbo, An unfitted finite element method, based on Nitsche's method, for elliptic interface problems, Comput. Methods Appl. Mech. Engrg. (2002) http://dx.doi.org/10.1016/S0045-7825(02)00524-8.

[13] J. Parvizian, A. Düster, E. Rank, Finite Cell Method: h- and p- extension for embedded domain methods in solid mechanics, Comput. Mech. 41 (2007) 122–133.

[14] D. Schillinger, E. Rank, An unfitted hp adaptive finite element method based on hierarchical B-splines for interface problems of complex geometry, Comput. Methods Appl. Mech. Engrg. 200(47–48 (2011) 3358–3380.

[15] D. Kamensky, M.-C. Hsu, D. Schillinger, J.A. Evans, A. Aggarwal, Y. Bazilevs, M.S. Sacks, T.J.R. Hughes, An immersogeometric variational framework for fluid–structure interaction: Application to bioprosthetic heart valves, Comput. Methods Appl. Mech. Engrg. 284 (2015) 1005–1053.

[16] D. Schillinger, M. Ruess, The Finite Cell Method: A review in the context of higher-order structural analysis of CAD and image-based geometric models, Arch. Comput. Methods Eng. 22 (3) (2015) 391–455.

[17] T. Jonsson, M.G. Larson, K. Larsson, Cut finite element methods for elliptic problems on multipatch parametric surfaces, Comput. Methods Appl. Mech. Engrg. 324 (2017) http://dx.doi.org/10.1016/j.cma.2017.06.018.

[18] F. de Prenter, C.V. Verhoosel, G.J. van Zwieten, E.H. van Brummelen, Condition number analysis and preconditioning of the finite cell method, Comput. Methods Appl. Mech. Engrg. 316 (2017) http://dx.doi.org/10.1016/j.cma.2016.07.006.

[19] T.J.R. Hughes, the Finite Element Method: Linear Static and Dynamic Finite Element Analysis, Dover Publications, Mineola, NY, 2000.

[20] J.S. Archer, Consistent mass matrix for distributed mass systems, J. Struct. Div. 89 (4) (1963) http://dx.doi.org/10.1061/jsdeag.0000939.

[21] L. Leidinger, Explicit Isogeometric B-Rep Analysis for Nonlinear Dynamic Crash Simulations (Ph.D. thesis), Technische Universität München, 2020.

[22] I. Harari, U. Albocher, Spectral investigations of Nitsche's method, Finite Elem. Anal. Des. 145 (2018) 20–31.

[23] E. Burman, S. Claus, P. Hansbo, M.G.M.-G. Larson, A. Massing, CutFEM: discretizing geometry and partial differential equations, Internat. J. Numer. Methods Engrg. 104 (7) (2015) 472–501, http://dx.doi.org/10.1002/nme.4823.

[24] E. Burman, Ghost penalty, C. R. Math. 348 (21–22) (2010) http://dx.doi.org/10.1016/j.crma.2010.10.006.

[25] S.K.F. Stoter, T.-H. Nguyen, R.R. Hiemstra, D. Schillinger, Variationally consistent mass scaling for explicit time-integration schemes of lower- and higher-order finite element methods, Comput. Methods Appl. Mech. Engrg. 399 (1) (2022) 115310, http://dx.doi.org/10.1016/j.cma.2022.115310, arXiv:2201.10475.

[26] T.-H. Nguyen, R.R. Hiemstra, S.K.F. Stoter, D. Schillinger, A variational approach based on perturbed eigenvalue analysis for improving spectral properties of isogeometric multipatch discretizations, Comput. Methods Appl. Mech. Engrg. 392 (2022) 114671, http://dx.doi.org/10.1016/j.cma.2022.114671, arXiv:2111.06501.

[27] A. Düster, J. Parvizian, Z. Yang, E. Rank, The Finite Cell Method for Three-Dimensional Problems of Solid Mechanics, Comput. Methods Appl. Mech. Engrg. 197 (2008) 3768–3782.

[28] C.V. Verhoosel, E.H. van Brummelen, S.C. Divi, F. de Prenter, Scan-based immersed isogeometric flow analysis, 2022, http://dx.doi.org/10.48550/ARXIV.2208.14994, URL https://arxiv.org/abs/2208.14994.

[29] S.C. Divi, C.V. Verhoosel, F. Auricchio, A. Reali, E.H. van Brummelen, Error-estimate-based adaptive integration for immersed isogeometric analysis, Comput. Math. Appl. 80 (11) (2020) http://dx.doi.org/10.1016/j.camwa.2020.03.026.

[30] M. Joulaian, S. Hubrich, A. Düster, Numerical integration of discontinuities on arbitrary domains based on moment fitting, Comput. Mech. 57 (6) (2016) 979–999.

[31] A. Abedian, A. Düster, Equivalent Legendre polynomials: Numerical integration of discontinuous functions in the finite element methods, Comput. Methods Appl. Mech. Engrg. 343 (2019) http://dx.doi.org/10.1016/j.cma.2018.08.002.

[32] M. Petö, W. Garhuom, F. Duvigneau, S. Eisenträger, A. Düster, D. Juhre, Octree-based integration scheme with merged sub-cells for the finite cell method: Application to non-linear problems in 3D, Comput. Methods Appl. Mech. Engrg. 401 (2022) 115565, http://dx.doi.org/10.1016/J.CMA.2022.115565.
[33] C.V. Verhoosel, G.J. Van Zwieten, B. Van Rietbergen, R. de Borst, Image-based goal-oriented adaptive isogeometric analysis with application to the micro-mechanical modeling of trabecular bone, Comput. Methods Appl. Mech. Engrg. 284 (2015) 138–164.
[34] J.L. Lions, E. Magenes, Non-Homogeneous Boundary Value Problems and Applications, 1973, http://dx.doi.org/10.1007/978-3-642-65393-3.
[35] E. Hinton, T. Rock, O.C. Zienkiewicz, A note on mass lumping and related processes in the finite element method, Earthq. Eng. Struct. Dyn. 4 (3) (1976) http://dx.doi.org/10.1002/eqe.4290040305.
[36] Y. Yang, H. Zheng, M.V. Sivaselvan, A rigorous and unified mass lumping scheme for higher-order elements, Comput. Methods Appl. Mech. Engrg. 319 (2017) http://dx.doi.org/10.1016/j.cma.2017.03.011.
[37] G. Strang, G.J. Fix, an Analysis of the Finite Element Method, first ed., Prentice-Hall, Englewood Cliffs, NJ, 1973.
[38] A.T. Patera, A spectral element method for fluid dynamics: Laminar flow in a channel expansion, J. Comput. Phys. 54 (3) (1984) http://dx.doi.org/10.1016/0021-9991(84)90128-1.
[39] A. Apostolatos, M. Breitenberger, R. Wüchner, K.U. Bletzinger, Domain decomposition methods and Kirchhoff-Love shell multipatch coupling in isogeometric analysis, in: Lecture Notes in Computational Science and Engineering, vol. 107, 2015, http://dx.doi.org/10.1007/978-3-319-23315-4_4.
[40] A.J. Herrema, E.L. Johnson, D. Proserpio, M.C. Wu, J. Kiendl, M.C. Hsu, Penalty coupling of non-matching isogeometric Kirchhoff–Love shell patches with application to composite wind turbine blades, Comput. Methods Appl. Mech. Engrg. 346 (2019) http://dx.doi.org/10.1016/j.cma.2018.08.038.
[41] T. Pasch, L.F. Leidinger, A. Apostolatos, R. Wüchner, K.U. Bletzinger, F. Duddeck, A priori penalty factor determination for (trimmed) NURBS-based shells with Dirichlet and coupling constraints in isogeometric analysis, Comput. Methods Appl. Mech. Engrg. 377 (2021) http://dx.doi.org/10.1016/j.cma.2021.113688.
[42] J.W. Barrett, C.M. Elliott, Fitted and unfitted finite-element methods for elliptic equations with smooth interfaces, IMA J. Numer. Anal. 7 (3) (1987) http://dx.doi.org/10.1093/imanum/7.3.283.
[43] L. Coradello, J. Kiendl, A. Buffa, Coupling of non-conforming trimmed isogeometric Kirchhoff–Love shells via a projected super-penalty approach, Comput. Methods Appl. Mech. Engrg. 387 (2021) http://dx.doi.org/10.1016/j.cma.2021.114187.
[44] J. Nitsche, Über ein Variationsprinzip zur Lösung von Dirichlet-Problemen bei Verwendung von Teilräumen, die keinen Randbedingungen unterworfen sind, in: Abhandlungen Aus Dem Mathematischen Seminar Der UniversitäT Hamburg, vol. 36, Springer, 1971, pp. 9–15.
[45] H.J. Barbosa, T.J. Hughes, The finite element method with Lagrange multipliers on the boundary: circumventing the Babuška-Brezzi condition, Comput. Methods Appl. Mech. Engrg. (1991) http://dx.doi.org/10.1016/0045-7825(91)90125-P.
[46] R. Stenberg, On some techniques for approximating boundary conditions in the finite element method, J. Comput. Appl. Math. (1995) http://dx.doi.org/10.1016/0377-0427(95)00057-7.
[47] J. Dolbow, I. Harari, An efficient finite element method for embedded interface problems, Internat. J. Numer. Methods Engrg. (2009) http://dx.doi.org/10.1002/nme.2486.
[48] T. Warburton, J.S. Hesthaven, On the constants in hp-finite element trace inverse inequalities, Comput. Methods Appl. Mech. Engrg. (2003) http://dx.doi.org/10.1016/S0045-7825(03)00294-9.
[49] F. de Prenter, C. Lehrenfeld, A. Massing, A note on the stability parameter in Nitsche's method for unfitted boundary value problems, Comput. Math. Appl. 75 (12) (2018) http://dx.doi.org/10.1016/j.camwa.2018.03.032.
[50] K. Höllig, U. Reif, Nonuniform web-splines, Comput. Aided Geom. Design 20 (5) (2003) http://dx.doi.org/10.1016/S0167-8396(03)00045-1.
[51] S. Badia, F. Verdugo, A.F. Martín, The aggregated unfitted finite element method for elliptic problems, Comput. Methods Appl. Mech. Engrg. 336 (2018) http://dx.doi.org/10.1016/j.cma.2018.03.022.
[52] S.C. Divi, P.H. Van Zuijlen, T. Hoang, F. De Prenter, F. Auricchio, A. Reali, E.H. Van Brummelen, C.V. Verhoosel, Residual-based error estimation and adaptivity for stabilized immersed isogeometric analysis using truncated hierarchical B-splines, J. Mech. 38 (2022) 204–237, http://dx.doi.org/10.1093/JOM/UFAC015, arXiv:2202.08763 URL https://academic.oup.com/jom/article/doi/10.1093/jom/ufac015/6593152.
[53] S. Badia, E. Neiva, F. Verdugo, Linking ghost penalty and aggregated unfitted methods, Comput. Methods Appl. Mech. Engrg. 388 (2022) http://dx.doi.org/10.1016/j.cma.2021.114232.
[54] Q. Deng, V.M. Calo, A boundary penalization technique to remove outliers from isogeometric analysis on tensor-product meshes, Comput. Methods Appl. Mech. Engrg. 383 (2021) http://dx.doi.org/10.1016/j.cma.2021.113907.
[55] M.G. Larson, S. Zahedi, Conservative Discontinuous Cut Finite Element Methods, 2021, http://dx.doi.org/10.48550/ARXIV.2105.02202, arXiv preprint arXiv:2105.02202.
[56] E. Burman, P. Hansbo, M.G. Larson, Explicit Time Stepping for the Wave Equation using CutFEM with Discrete Extension, SIAM J. Sci. Comput. 44 (3) (2022) A1254–A1289, http://dx.doi.org/10.1137/20M137937X.
[57] R. Szilard, Theories and Applications of Plate Analysis: Classical, Numerical and Engineering Methods, Appl. Mech. Rev. 57 (6) (2004) http://dx.doi.org/10.1115/1.1849175.
[58] J.R. Vinson, S. Abrate, The Behavior of Thin Walled Structures, Beams, Plates, and Shells, J. Appl. Mech. 57 (4) (1990) http://dx.doi.org/10.1115/1.2897641.
[59] Y. Cai, J. Chen, N. Wang, A Nitsche extended finite element method for the biharmonic interface problem, Comput. Methods Appl. Mech. Engrg. 382 (2021) http://dx.doi.org/10.1016/j.cma.2021.113880.

[60] J.A. Cottrell, A. Reali, Y. Bazilevs, T.J. Hughes, Isogeometric analysis of structural vibrations, Comput. Methods Appl. Mech. Engrg. 195 (41–43) (2006) http://dx.doi.org/10.1016/j.cma.2005.09.027.

[61] M. Bischoff, K.-U. Bletzinger, W.A. Wall, E. Ramm, Models and Finite Elements for Thin-Walled Structures, in: Encyclopedia of Computational Mechanics, 2004, http://dx.doi.org/10.1002/0470091355.ecm026.

[62] J. Benzaken, J.A. Evans, S.F. McCormick, R. Tamstorf, Nitsche's method for linear Kirchhoff–Love shells: Formulation, error analysis, and verification, Comput. Methods Appl. Mech. Engrg. 374 (2021) http://dx.doi.org/10.1016/j.cma.2020.113544.

[63] G.J. van Zwieten, J. van Zwieten, C.V. Verhoosel, E. Fonn, T.M. van Opstal, W. Hoitinga, Nutils 7.0, http://dx.doi.org/10.5281/zenodo.6006701.